Morphological, molecular, and functional evidence for a CNS-like oral nerve ring in the sea anemone *Nematostella vectensis*

Authors

Ruohan Zhong, Chris W. Seidel, Anna M.L. Klompen, Matthew C. Gibson

Affiliations

Stowers Institute for Medical Research, Kansas City, MO, USA

Correspondence

Matthew C. Gibson (mg2@stowers.org)

Abstract

The emergence of centralized nervous systems reflects a major inflection point in evolution, enabling animals to integrate diverse inputs and coordinate complex behaviors. Neural centralization is typically associated with Bilateria, whereas their sister group, Cnidaria (jellyfish, anemones, and corals), has long been thought to rely on diffuse nerve nets mediating simple reflexes[1–4]. This view, reinforced by limited anatomical and molecular data, has left unresolved whether cnidarians can form localized centers for neural processing, a question sharpened by the growing recognition of their diverse behavioral repertoires[5–8]. Here we show that the sea anemone *Nematostella vectensis* possesses an oral nerve ring composed of ganglion-like condensations, a hallmark of centralized organization. These neurons are enriched for excitatory, inhibitory, and modulatory receptors but lack sensory or ciliary markers, yielding a molecular profile most consistent with bilaterian interneurons. Genetic disruption of a conserved inhibitory receptor subunit predominantly expressed in the oral nerve ring delayed the initiation of swallowing in a novel feeding paradigm, demonstrating a potential role in behavioral regulation. Together, these findings provide converging anatomical, molecular, and functional evidence that cnidarians can assemble localized integrative centers, suggesting that key elements of neural centralization predated the cnidarian–bilaterian split.

Introduction

Animals coordinate behavior by concentrating neurons into localized integrative centers, a strategy exemplified by the bilaterian central nervous system (CNS). In contrast, cnidarians, the sister group to bilaterians, are traditionally portrayed as relying on diffuse nerve nets that mediate simple reflexes[1–4] (Fig. 1a). This dichotomy has long framed centralization as a bilaterian innovation and left unresolved whether cnidarians can assemble structures that support local integrative processing.

The diffuse nerve net paradigm has persisted for over a century, in part due to assumptions tied to cnidarians' basal phylogenetic position, the absence of macroscopic brain- or nerve cord-like structures, and a lack of molecular tools to visualize and classify neurons. *Hydra*, long the principal model for cnidarian neurobiology, further shaped this view through its diffuse, highly regenerative but lineage-specific neural organization[9,10]. Within this framework, cnidarian nerve nets were widely interpreted as morphologically and functionally simple. Still, classical anatomical studies hint that this picture might be incomplete. In 1879, Oscar and Richard Hertwig described a high density of neural elements arranged in crisscross and radial patterns in the oral disc of the parasitic anemone *Calliactis*[11]. In 1963, Elaine Robson illustrated radial oral nerve tracts in the swimming anemone *Stomphia* and proposed that they mediate coordination between the oral disc and the mesenteries[12]. In 1982, Kinnamon and Westfall identified interneuron-like cells at hypostome–tentacle junctions in *Hydra littoralis*, which they referred to as "primitive ganglia"[13]. These findings raise the possibility of localized neural organization within cnidarian nerve nets, although their cellular identities, developmental origins, and functional roles remain unknown.

Modern behavioral work strengthens this perspective by revealing functional specialization across cnidarian lineages. *Clytia hemisphaerica* relies on spatially organized subnetworks to coordinate food handling[5]; *Hydra vulgaris* displays satiety-dependent behaviors mediated by enteric- and CNS-like neuronal subpopulations[8]; the box jellyfish *Tripedalia cystophora* can modify obstacle avoidance through operant conditioning[7]; and the sea anemone *Nematostella vectensis* exhibits circadian

locomotion and associative learning[6,14]. Together, these findings indicate that cnidarian nerve nets support more structured and context-dependent processing than is captured by the classical diffuse nerve net paradigm.

Nematostella vectensis offers an ideal system to revisit these assumptions with modern tools. It combines a tractable life cycle[15,16], a well-annotated genome[17–19], and an expanding molecular toolkit[20–22]. Unlike bilaterian invertebrates such as *Drosophila* or *C. elegans*, which have undergone extensive gene loss, *Nematostella* retains a broad ancestral eumetazoan gene repertoire more comparable to vertebrates, including synaptic machinery, neurotransmitter pathways, and developmental regulators[23–30]. Despite its compact genome (269.4 Mb; ~19,200 protein-coding genes, similar to humans), our analysis of the current RefSeq assembly reveals an unexpectedly broad diversification of neurotransmitter receptor families, including glutamate, γ-aminobutyric acid (GABA), acetylcholine, monoamine, and neuropeptide receptors, well beyond the two previously characterized types[31,32] and far exceeding the diversity seen in many bilaterians (Supplementary Table 2). In contrast, receptor numbers for other signaling pathways such as BMP[33], Wnt[34], and Hedgehog[35] are comparable to or below human levels, suggesting that this diversification is specific to neural communication genes. Developmentally, *Nematostella* exhibits bilateral patterning of tentacles, musculature, and Hox/BMP expression along its directive axis[22,33,36], undermining the traditional association between radial body plans and diffuse neural organization.

Whether cnidarians can assemble discrete interneuron-like centers capable of local integrative processing has remained unclear. Here, using anatomical, molecular, and functional approaches, we examine nervous system organization in the cnidarian *Nematostella vectensis* and assess whether features associated with neural centralization extend deeper in animal evolution than previously appreciated.

Results

Motor coordination during feeding

Feeding, an innate, essential, and readily inducible behavior requiring whole-body coordination, provides a tractable entry point to test whether a cnidarian nerve net contains localized neural structures that support complex motor transitions. To characterize feeding under ecologically relevant conditions, we recorded adult *Nematostella* polyps partially burrowed in gravel with the oral disc exposed above the substrate (Fig. 1b). Upon introduction of free-swimming *Artemia* nauplii (brine shrimp larvae), tentacles that made contact bent, twisted, and captured prey, whereas non-contacting tentacles remained poised in the background. Prey-bearing tentacles then contracted toward the oral opening, conveying food through the pharynx and into the body cavity (Supplementary Video 1).

In initial experiments, we found that feeding responses were highly flexible and context dependent, varying with prey size, number, position, and mode of delivery (Supplementary Videos 2–5 and Extended Data Fig. 5f). To identify the core elements within this behavioral diversity, we established a simplified feeding paradigm in which a cylindrical egg-white pellet (1 mm × 1 mm) was gently delivered to the oral disc using a cat whisker (Fig. 1c,d and Supplementary Video 6). This consistently triggered a reproducible sequence of motor subroutines involving distinct body regions. We defined two stereotyped phases: (1) grasping, from the first tentacle-driven movement to the onset of neck constriction, during which tentacles sense and ensnare the pellet, pull it toward the mouth, and clasp around it; and (2) swallowing, from the onset of neck constriction until the pellet reaches the distal end of the pharynx, characterized by rhythmic neck contractions, mouth opening and closing, food passage through the pharynx, and temporary suspension of oral-to-aboral peristalsis. Our observations thus demonstrate that *Nematostella* executes a structured, multi-step feeding program despite lacking any obvious anatomical centralization.

Anatomical organization of the oral nerve net

The adaptability and robustness of feeding under varied conditions raise the question of how coordinated behaviors can be directed by a diffuse nerve net. In *Nematostella*, a previously described *NvElav1* reporter labels neurons along the body column[25] but

shows little expression in neurons of the oral disc and tentacles. To overcome this limitation, we generated additional reporter lines by screening promoters of candidate genes identified in scRNA-seq data[28].

Among them, a 1.9 kb upstream fragment of the *Nematostella SH3GL3* (Endophilin-A3) homolog drove a fluorescent reporter *NvSH3GL3*^{P}*>mScarlet-I* (Extended Data Fig. 1b) that robustly labeled neurons, including dense innervation of the oral disc and tentacles, major structures involved in feeding (Fig. 1e). Notably, this pattern resembles early hand-drawn descriptions of oral neuronal condensations in other sea anemones[11,12], suggesting that it may represent a conserved anatomical feature.

High-resolution imaging of the oral region revealed that neuronal organization is not diffuse but rather exhibits pronounced spatial patterning in both soma distribution and neurite orientation (Fig. 1e). Neurons with enlarged somata and multipolar morphology clustered at tentacle junctions, where they gave rise to prominent circumferential neurite bundles that together formed a ring-like structure. We refer to this neuronal structure as the oral nerve ring (ONR). In contrast, other oral neurons exhibited smaller somata and distinct projection orientations, including radially oriented neurites around the mouth and longitudinal projections within the tentacles (Fig. 1e). With circumferential neurites linking tentacles and localization at the interface between the tentacles, pharynx, and body column, the ONR occupies a position well suited for coordinating activity across multiple body regions.

To examine how this circumoral organization arises, we analyzed *NvSH3GL3*^{P}-labeled neurons during larval-to-polyp transitions associated with tentacle formation (Extended Data Fig. 1a,c). In late planula larvae, neurons with enlarged somata were present but sparsely distributed within the oral ectoderm and did not exhibit a coherent ring-like arrangement. As animals progressed through the tentacle-bud stage and into primary polyps, the number of these ONR neurons increased, accompanied by higher neurite density and preferential localization to tentacle junctions (Extended Data Fig. 1c). With further growth and the sequential addition of tentacles[36], this process gave rise to a

157 progressively denser circumoral neurite bundle and an increased accumulation of large
158 neuronal somata at tentacle junctions, ultimately forming a clearly defined oral nerve
159 ring (Extended Data Fig. 1d). These observations indicate that ONR organization
160 emerges gradually during development and scales with increasing body size and
161 morphological complexity.
162
163 **Molecular diversity of the oral nerve net**
164 Building on the anatomical and developmental characterization of the oral nerve ring,
165 we next examined its molecular composition to assess potential functional
166 specialization. Oral discs from adult *NvSH3GL3*^{P} reporter animals were dissected, and
167 mScarlet-I-positive cells were enriched by fluorescence-activated cell sorting (FACS)
168 prior to single-cell RNA sequencing using the 10x Genomics platform (Fig. 2a). This
169 yielded 3,297 cells comprising both neural and non-neural populations (Fig. 2b), as
170 defined by marker gene expression (Fig. 2c). Specifically, neural clusters expressed
171 canonical neuronal markers (*ELAV*, *achaete-scute*), synaptic machinery (*synapsin*,
172 *synaptotagmin*, *endophilin*, vesicular transporters), as well as cytoskeletal proteins, ion
173 channels, transporters, and adhesion/signaling molecules (Fig. 2c and Extended Data
174 Fig. 2a). Expression of the *NvSH3GL3*^{P} reporter closely paralleled endogenous
175 *NvSH3GL3* across neural clusters, supporting the fidelity of the reporter. In contrast,
176 non-neural clusters expressed the endogenous red fluorescent protein *NvFP-7R*[37]
177 together with tissue-associated cytoskeletal and extracellular-matrix genes, providing an
178 internal reference for non-neural identity (Fig. 2c).
179
180 To examine the spatial expression of markers enriched in specific transcriptional
181 clusters, we analyzed four-tentacle primary polyps (7–10 days post-fertilization, dpf),
182 which are more amenable to whole-mount fluorescent in situ hybridization (FISH) and
183 confocal imaging than adult tissues. Markers enriched in cluster 3 consistently localized
184 to the pharyngeal region (Fig. 2d,e). In contrast, markers enriched in clusters 5 and 6
185 localized predominantly to the ectoderm of the oral disc and tentacles (Fig. 2f,g and
186 Extended Data Fig. 2b–e). Together, these findings show that at least a subset of

187 transcriptionally defined neural clusters within the oral nerve net exhibit clear spatial
188 correlates across oral tissues, linking molecular identity to anatomical position.
189
190 **Interneuron-like molecular features of the oral nerve ring**
191 We next examined the molecular diversity of oral neurons, as reflected in their sensory
192 transduction components and neurotransmitter receptor repertoires, to assess whether
193 transcriptionally defined populations exhibit features consistent with functional
194 specialization. Sensory-related genes included acid-sensing ion channels (ASICs),
195 transient receptor potential (TRP) channels, opsins, and cilia-associated proteins
196 (CFAPs, DNAHs, and RSPs). Neurotransmitter receptors fell into three classes:
197 excitatory (ionotropic glutamate, acetylcholine), inhibitory (ionotropic GABA, glycine),
198 and modulatory (metabotropic glutamate, acetylcholine, GABA, monoamines,
199 neuropeptides). Full gene lists are provided in Supplementary Table 2.
200
201 Comparison across transcriptional clusters revealed that clusters 5 and 6 were
202 distinguished by low sensory gene expression and broad representation of excitatory
203 (E), inhibitory (I), and modulatory (M) receptor classes (Fig. 3a). Co-expression analysis
204 showed that the majority of cells within these clusters simultaneously expressed
205 receptors from all three classes (Fig. 3b and Extended Data Fig. 3), indicating a
206 molecular profile consistent with integrative signal processing rather than sensory
207 specialization, reminiscent of integrative interneurons in the bilaterian CNS. This
208 molecular profile also parallels two morphological features observed in ONR neurons
209 labeled by the *NvSH3GL3*^{P} reporter, including the absence of sensory cilia and the
210 presence of ganglion-like neuronal condensations. Although clusters 5 and 6 shared
211 these general characteristics, their receptor compositions diverged. Cluster 5 exhibited
212 substantial heterogeneity in E/I/M receptor combinations, whereas cluster 6 displayed a
213 more uniform and balanced receptor profile across cells (Fig. 3c). This balance,
214 approximately 20–30–50 in the relative proportions of excitatory, inhibitory, and
215 modulatory receptor expression per cell, was maintained despite variation in receptor
216 identity, suggesting functional convergence within cluster 6.
217

Other neural clusters showed receptor diversity but lacked this integrative signature. Cluster 9 expressed receptors from all three classes; however, most cells were single- or double-positive per cell and were also enriched for sensory and ciliary genes, suggesting a sensory role. Clusters 11, 12, and 14 exhibited broad modulatory repertoires, with some cells expressing more than 20 receptor types, yet none showed the balanced E/I/M profile characteristic of clusters 5 and 6 (Fig. 3a–c).

Marker analysis further reinforced these distinctions (Fig. 3d). Clusters 5 and 6 shared transcription factors including *POU4/Brn3*[29], *Orthopedia (Otp)*, and *SIX3/6*[27], which are known to regulate anterior CNS patterning and neuronal specification in Bilateria[38–40]. Although *SIX3/6* expression is restricted to the aboral pole in *Nematostella* larvae[27], it was enriched in adult oral disc neurons (Extended Data Fig. 2b). Both clusters also expressed multiple ionotropic GABA receptor-like subunits, with shared and cluster-specific paralogs (Fig. 3d and Fig. 5a), indicating subtype-specific inhibitory tuning. In contrast, cluster 2 showed broad neuronal gene expression without defining markers, consistent with an undifferentiated state. Other clusters (11, 12, 14) were characterized by distinct modulatory receptor expression (Extended Data Fig. 4a) and co-expression of a broad range of neurotransmitter receptors, with modulatory types especially prominent, together with ciliary and sensory genes (Extended Data Fig. 4b–d). Together, these comparisons revealed clusters 5 and 6 as the most plausible ONR-associated neuronal populations within the broader oral neural domain, based on their spatial localization and interneuron-like molecular profiles.

To identify molecular markers within clusters 5 and 6 that label ONR neurons, we performed FISH on four-tentacle primary polyps for genes enriched in these clusters. Candidate genes were excluded from further consideration if they fell into three categories that limited their utility as ONR markers: (1) genes enriched in the adult oral disc scRNA-seq dataset but weak or undetectable in primary polyps (Extended Data Fig. 2b); (2) transcripts detected in ONR-like cells but also expressed broadly along the body column (Extended Data Fig. 2c,d); and (3) transcripts confined to the oral end but either diffusely expressed across tissues or localized to cells lacking the large somata

249 and tentacle-junction positioning characteristic of ONR neurons (Extended Data Fig.
250 2e). By contrast, multiple ionotropic GABA receptor-like ($GABA_AR$-like) subunits
251 satisfied both transcriptional enrichment and anatomical localization criteria, with
252 expression concentrated in the oral region and in cells with ONR-like morphology (Fig.
253 2g, Fig. 5b and Extended Data Fig. 2d). Although no single gene exclusively marked the
254 entire ONR, these results highlight GABA signaling as a promising entry point for
255 molecular and functional interrogation of the ONR.
256
257 **GABAergic pathway in the oral nerve net**
258 Building on this molecular signature, we asked whether the ONR contains the core
259 components of GABAergic signaling. In bilaterians, canonical GABAergic signaling
260 involves four key elements: synthesis by glutamate decarboxylase (GAD), vesicular
261 packaging by vesicular GABA transporter (VGAT), reception through ionotropic or
262 metabotropic GABA receptors, and clearance by GABA transporter (GAT)[41]. To assess
263 whether *Nematostella* possesses a comparable pathway architecture, we combined
264 immunohistochemistry, single-cell and bulk transcriptomics, and comparative genomics.
265
266 Whole-mount immunostaining of *NvSH3GL3*^{P}*>mScarlet-I* primary polyps revealed
267 widespread GABA immunoreactivity, with strong enrichment at the oral end (Fig. 4a).
268 Within the oral disc, a subset of GABA-positive cells overlapped with mScarlet-I-positive
269 neurons possessing large somata characteristic of ONR morphology (Fig. 4b),
270 suggesting that ONR neurons may both release and respond to GABA.
271
272 In our scRNA-seq dataset, among vesicular inhibitory amino acid transporter
273 (VIAAT) homologs, only a single homolog showed substantial expression in adult oral
274 neurons (LOC5506413; hereafter *VGAT*). Multiple $GABA_AR$-like subunits showed
275 expression largely confined to clusters 5 and 6 (Fig. 3d). Individual cells co-expressed
276 1–10 subunits (Fig. 3a), a combinatorial diversity rarely seen in invertebrates but
277 characteristic of the vertebrate CNS[41,42]. Subunits displayed broad to cluster-specific
278 distributions, with mutually exclusive, partially overlapping, or nested expression
279 patterns (Fig. 5a), consistent with cell type-specific receptor assemblies. Notably,

280 approximately 50% of cluster 5 neurons and 75% of cluster 6 neurons co-expressed
281 $GABA_AR$(s) and *VGAT* (Extended Data Fig. 5a), a defining feature of inhibitory
282 interneurons capable of both releasing and responding to GABA[41]. Some $GABA_AR$-
283 positive neurons lacked *VGAT*, likely representing postsynaptic targets of inhibition.
284 Together, these findings indicate that the ONR supports a GABAergic signaling
285 architecture encompassing both presynaptic and postsynaptic components, with
286 receptor diversity suggesting a capacity for fine-tuned inhibition comparable to bilaterian
287 central circuits.
288
289 To complement the single-cell RNA-seq data, we used bulk RNA-seq to transcriptionally
290 profile the adult tentacles, oral disc, pharynx, and oral body wall. This approach
291 provided deeper and less biased transcript coverage across whole tissues than scRNA-
292 seq restricted to FACS-enriched oral neurons. $GABA_AR$-like transcripts showed highest
293 relative expression in the oral disc and tentacles, mirroring GABA immunostaining and
294 reinforcing the receptor diversity of the oral nerve net (Fig. 4c).
295
296 Prompted by this enrichment, we surveyed the full *Nematostella* $GABA_AR$-like gene set.
297 Here, we use "$GABA_AR$-like" to denote subunits with sequence similarity to bilaterian
298 $GABA_A$ or glycine receptor subunits, as detailed in the Methods. Genomic analysis
299 identified 40 distinct subunits in *Nematostella*—exceeding the 2–23 typical of bilaterians
300 (Fig. 4d and Supplementary Table 3). Phylogenetic analysis across 13 species (7
301 cnidarians and 6 bilaterians; Supplementary Table 4) supported a single ancestral
302 $GABA_AR$, with subsequent expansions in both lineages (Fig. 4e and Supplementary Fig.
303 1). In *Nematostella,* only three subunits clustered with bilaterian orthologs, whereas the
304 remaining 37 arose from anthozoan-specific duplications, generating a lineage-specific
305 expansion that underpinned ONR receptor diversity. A recent preprint reported a similar
306 cnidarian-specific radiation based on narrower taxon sampling (2 cnidarians and 3
307 bilaterians) and functional assays of selected subunits[43]. Although metabotropic GABA
308 receptors are also expanded (12 in *Nematostella* vs. 2 in humans; Supplementary Table
309 3), their expression was scattered across neural and non-neural clusters without ONR

310 enrichment; therefore, we focused on ionotropic receptors as the core ONR-associated
311 repertoire.
312
313 Despite the presence of both plasma membrane (GAT) and vesicular (VGAT/VIAAT)
314 GABA transporters, and a diverse repertoire of GABA receptors, we did not identify a
315 canonical *GAD* homolog enriched in neuronal populations within the oral scRNA-seq
316 dataset. Ten putative *GAD*-like candidates, including two reported previously[44,45],
317 showed no enrichment in any neuronal cluster and were instead weakly or sparsely
318 expressed in a small number of non-neural clusters (Supplementary Information). These
319 findings suggest that GABA production in *Nematostella* may rely on non-canonical or
320 lineage-divergent pathways.
321
322 **A $GABA_A$ receptor-like subunit regulates swallowing initiation**
323 The molecular profiling described above highlights GABA signaling as central to ONR
324 function. Among the 40 $GABA_AR$-like homologs encoded in the *Nematostella* genome,
325 we focused on *NvGABAAR1* (LOC5505184), which showed the broadest expression
326 within cluster 5 and the highest transcript levels (Fig. 5a). *NvGABAAR1* was also co-
327 expressed with *VGAT*, a canonical feature of inhibitory interneurons. Moreover, it was
328 one of only three $GABA_AR$ subunits that clustered with bilaterian orthologs (Fig. 4e), and
329 AlphaFold modeling revealed strong structural similarity to human GABRR3 (Fig. 4f and
330 Extended Data Fig. 5c). Crucially, FISH confirmed that *NvGABAAR1* was expressed in
331 oral disc neurons with large somata and circumferential neurites, consistent with ONR
332 morphology, although expression was also observed in a subset of tentacle neurons
333 (Fig. 5b).
334
335 To test the function of *NvGABAAR1*, we used CRISPR/Cas9 mutagenesis to introduce
336 a +27 bp insertion, generating a premature stop codon in the ligand-binding domain
337 (Extended Data Fig. 5b). Homozygous *NvGABAAR1*$^{+27/+27}$ animals were viable and
338 displayed no overt neural or developmental defects (Fig. 5c).
339

340 We next assayed the behavior of *NvGABAAR1*$^{+27/+27}$ mutants using our standardized
341 feeding paradigm. Animals were sequentially presented with four sham prey items (1
342 mm × 1 mm egg-white pellets), and grasping and swallowing durations were quantified
343 (Fig. 5d). Grasping duration, defined as the interval from the first tentacle-driven
344 movement to the onset of neck constriction (Fig. 1d), did not differ between wild-type
345 (WT) and mutant animals ($p = 0.35$), indicating intact prey detection and initial motor
346 responses (Fig. 5e). Grasping duration was also stable across repeated trials for both
347 genotypes, with no evidence of systematic drift over ten consecutive presentations
348 (Extended Data Fig. 5d).
349
350 By contrast, swallowing showed a genotype-dependent effect restricted to the first of
351 four feeding trials (Fig. 5f). Linear mixed-effects modeling revealed a significant
352 genotype × trial interaction. Strikingly, WT animals showed stable swallowing durations
353 across trials, whereas mutants exhibited a delay on the first feeding trial (46 ± 10 s; $p <$
354 0.001) and were indistinguishable from WT on subsequent trials (all $p > 0.2$).
355 Importantly, including food-delivery method (pipette vs whisker) or starvation level as
356 covariates did not alter the genotype × trial interaction, indicating that the delay on trial 1
357 reflects a robust, intrinsic deficit in swallowing initiation rather than an effect of stimulus
358 delivery or feeding state. Mutant animals recovered rapidly after the initial trial and
359 maintained WT-like swallowing durations for the remainder of the assay, a pattern that
360 persisted for at least nine consecutive trials (Extended Data Fig. 5e). Together, these
361 findings demonstrate that *NvGABAAR1* is specifically required for the initiation of
362 swallowing behavior, supporting a role for GABAergic signaling within the oral nerve net
363 in coordinating the transition from prey capture to ingestion and, potentially, the
364 engagement of feeding-related behavioral states.
365
366 **Discussion**
367 Cnidarian nerve nets have long been viewed as diffuse and reflexive, yet their capacity
368 for structured, context-dependent behaviors hints at deeper organization. Here we show
369 that the sea anemone *Nematostella vectensis* possesses an oral nerve ring (ONR), a
370 localized neural structure implicated in motor coordination during feeding. This finding

371 suggests that key elements of neural integration predate the cnidarian–bilaterian split
372 some 700 million years ago, extending the evolutionary roots of centralized
373 organization.
374
375 The ONR forms a localized aggregation of neuronal somata that meets classical criteria
376 for a ganglion-like structure. In bilaterians, ganglia are clusters of somata functioning as
377 local integrative or relay centers, whereas in cnidarians “ganglion cells” traditionally
378 refer to aciliate neurons positioned basally within the epithelium[2,25]. Unlike previously
379 described neurite condensations in cnidarian nerve nets[25,46,47], the ONR constitutes a
380 true ganglion-like aggregation of neuronal somata, providing the first modern evidence
381 of soma-level clustering in a cnidarian (Fig. 1e). We use “ganglion-like” here in the
382 morphological sense only, to describe neuronal clustering rather than positional
383 homology to bilaterian ganglia. This clustered architecture provides an anatomical basis
384 for a CNS-like site of integration within a diffuse nerve net. ONR neurons display
385 morphological diversity, including bipolar and tripolar forms, suggesting heterogeneity in
386 connectivity and function. Developmentally, the ONR arises from initially scattered
387 neurons that progressively cluster as polyps grow (Extended Data Fig. 1c,d). This
388 scaling of organization with body size and muscular compartmentalization may reflect
389 an adaptive route toward more efficient long-range coordination, a pattern that parallels
390 proposed evolutionary transitions from diffuse to centralized networks across early
391 metazoans[4]. While postsynaptic partners remain unmapped, the ONR’s position and
392 organization indicate an interneuron-like hub mediating sensory–motor coordination.
393
394 Molecular and functional evidence support an interneuron-like identity for ONR neurons.
395 Single-cell analyses show that ONR neurons lack sensory markers but express a
396 combinatorial set of excitatory, inhibitory, and modulatory receptors together with
397 transcription factors typical of bilaterian interneurons (Fig. 3a–d). This transcriptional
398 profile defines a CNS-like integrative module, in which prominent inhibitory components,
399 including GABA-immunoreactive somata, a vesicular GABA transporter, and an
400 expanded suite of $GABA_A$ receptor-like subunits, form a molecular framework for
401 regulating excitation balance and temporal precision[41]. Although comprehensive

402 functional mapping of the ONR remains beyond the scope of this study, our functional
403 perturbation of an ONR-enriched $GABA_AR$ subunit selectively delayed the onset of
404 swallowing behavior without impairing prey detection or grasping (Fig. 5e,f). The delay
405 was most evident during the first feeding event but normalized by the second trial,
406 indicating rapid behavioral recovery once feeding was initiated. This transient
407 phenotype suggests that the ONR contributes to the timing and coordination of motor
408 transitions during the initial stages of feeding rather than executing the motor output
409 itself. Future work may uncover how internal physiological states shape ONR-mediated
410 coordination. Together, these observations point to a role for inhibitory signaling within
411 the ONR in modulating behavioral sequence progression, a hallmark of integrative
412 rather than purely reflexive circuits.
413
414 Intriguingly, ONR neurons also expressed *SIX3/6* and *Orthopedia* (Fig. 3d), two broadly
415 conserved transcription factors that in bilaterians regulate anterior CNS patterning and
416 neuroendocrine specification[39,40]. These findings suggest that transcriptional programs
417 defining the bilaterian anterior neuroectoderm may have deep evolutionary roots in the
418 patterning of neural condensations around feeding structures.
419
420 Collectively, our results position the *Nematostella* oral nerve ring as an intermediate
421 level of neural organization between diffuse nerve nets and centralized nervous
422 systems. Its architecture exemplifies how clusters of interneuron-like cells can enable
423 coordination without a bona fide brain. The marked expansion of neurotransmitter
424 receptors (Supplementary Table 2) underscores molecular elaboration as a route to
425 circuit flexibility in early animals, perhaps through receptor repurposing or adaptive
426 tuning to estuarine variability. While it remains unresolved whether the *Nematostella*
427 ONR and bilaterian CNS share a common origin or represent convergent solutions, their
428 shared features reveal deep evolutionary continuity in the principles of neural
429 integration.
430

References

1. Bullock, T. & Horridge, G. A. *Structure and Function in the Nervous Systems of Invertebrates.* (1965).
2. Grimmelikhuijzen, C. P. & WestfalP, J. A. The nervous systems of Cnidarians. (1995).
3. Holland, L. Z. *et al.* Evolution of bilaterian central nervous systems: a single origin? *EvoDevo* **4**, 27 (2013).
4. Arendt, D., Tosches, M. A. & Marlow, H. From nerve net to nerve ring, nerve cord and brain — evolution of the nervous system. *Nat. Rev. Neurosci.* **17**, 61–72 (2016).
5. Weissbourd, B. *et al.* A genetically tractable jellyfish model for systems and evolutionary neuroscience. *Cell* **184**, 5854-5868.e20 (2021).
6. Botton-Amiot, G., Martinez, P. & Sprecher, S. G. Associative learning in the cnidarian *Nematostella vectensis*. *Proc. Natl. Acad. Sci.* **120**, e2220685120 (2023).
7. Bielecki, J., Dam Nielsen, S. K., Nachman, G. & Garm, A. Associative learning in the box jellyfish Tripedalia cystophora. *Curr. Biol.* **33**, 4150-4159.e5 (2023).
8. Giez, C. *et al.* Satiety controls behavior in Hydra through an interplay of pre-enteric and central nervous system-like neuron populations. *Cell Rep.* **43**, 114210 (2024).
9. Galliot, B. Hydra, a fruitful model system for 270 years. *Int. J. Dev. Biol.* **56**, 411–423 (2012).
10. Keramidioti, A. *et al.* A new look at the architecture and dynamics of the Hydra nerve net. Preprint at https://doi.org/10.7554/eLife.87330.2 (2024).
11. Hertwig, O. & Hertwig, R. K. W. T. von R. K. W. T. von H. S. *Die Actinien : Anatomisch Und Histologisch, Mit Besanderer Berücksichtigung Des Nervenmuskelsystems*. vol. Hft.1 (G. Fischer, Jena, 1879).
12. Robson, E. A. The nerve-net of a swimming anemone, Stomphia coccinea. *J. Cell Sci.* **S3-104**, 535–549 (1963).
13. Kinnamon, J. C. & Westfall, J. A. Types of neurons and synaptic connections at hypostome-tentacle junctions in *Hydra*. *J. Morphol.* **173**, 119–128 (1982).
14. Oren, M. *et al.* Profiling molecular and behavioral circadian rhythms in the non-symbiotic sea anemone Nematostella vectensis. *Sci. Rep.* **5**, 11418 (2015).

15. Layden, M. J., Rentzsch, F. & Röttinger, E. The rise of the starlet sea anemone *Nematostella vectensis* as a model system to investigate development and regeneration. *WIREs Dev. Biol.* **5**, 408–428 (2016).
16. Carvalho, J. E., Burtin, M., Detournay, O., Amiel, A. R. & Röttinger, E. Optimized husbandry and targeted gene-editing for the cnidarian *Nematostella vectensis*. *Development* **152**, (2025).
17. Putnam, N. H. *et al.* Sea Anemone Genome Reveals Ancestral Eumetazoan Gene Repertoire and Genomic Organization. *Science* **317**, 86–94 (2007).
18. Zimmermann, B. *et al.* Topological structures and syntenic conservation in sea anemone genomes. *Nat. Commun.* **14**, 8270 (2023).
19. Fletcher, C. *et al.* The genome sequence of the starlet sea anemone, Nematostella vectensis (Stephenson, 1935). *Wellcome Open Res.* **8**, 79 (2023).
20. Ikmi, A., McKinney, S. A., Delventhal, K. M. & Gibson, M. C. TALEN and CRISPR/Cas9-mediated genome editing in the early-branching metazoan Nematostella vectensis. *Nat. Commun.* **5**, (2014).
21. Renfer, E. & Technau, U. Meganuclease-assisted generation of stable transgenics in the sea anemone Nematostella vectensis. *Nat. Protoc.* **12**, 1844–1854 (2017).
22. He, S. *et al.* An axial Hox code controls tissue segmentation and body patterning in *Nematostella vectensis*. *Science* **361**, 1377–1380 (2018).
23. Magie, C. R., Pang, K. & Martindale, M. Q. Genomic inventory and expression of Sox and Fox genes in the cnidarian Nematostella vectensis. *Dev. Genes Evol.* **215**, 618–630 (2005).
24. Anctil, M. Chemical transmission in the sea anemone Nematostella vectensis: A genomic perspective. *Comp. Biochem. Physiol. Part D Genomics Proteomics* **4**, 268–289 (2009).
25. Nakanishi, N., Renfer, E., Technau, U. & Rentzsch, F. Nervous systems of the sea anemone *Nematostella vectensis* are generated by ectoderm and endoderm and shaped by distinct mechanisms. *Development* **139**, 347–357 (2012).
26. Layden, M. J., Boekhout, M. & Martindale, M. Q. *Nematostella vectensis achaete-scute*homolog*NvashA*regulates embryonic ectodermal neurogenesis and represents

491 an ancient component of the metazoan neural specification pathway. *Development*
492 **139**, 1013–1022 (2012).
493 27. Sinigaglia, C., Busengdal, H., Leclère, L., Technau, U. & Rentzsch, F. The Bilaterian
494 Head Patterning Gene six3/6 Controls Aboral Domain Development in a Cnidarian.
495 *PLoS Biol.* **11**, e1001488 (2013).
496 28. Sebé-Pedrós, A. *et al.* Cnidarian Cell Type Diversity and Regulation Revealed by
497 Whole-Organism Single-Cell RNA-Seq. *Cell* **173**, 1520-1534.e20 (2018).
498 29. Tournière, O. *et al.* NvPOU4/Brain3 Functions as a Terminal Selector Gene in the
499 Nervous System of the Cnidarian Nematostella vectensis. *Cell Rep.* **30**, 4473-
500 4489.e5 (2020).
501 30. Cole, A. G. *et al.* Updated single cell reference atlas for the starlet anemone
502 Nematostella vectensis. *Front. Zool.* **21**, 8 (2024).
503 31. Faltine-Gonzalez, D. Z. & Layden, M. J. Characterization of nAChRs in Nematostella
504 vectensis supports neuronal and non-neuronal roles in the cnidarian–bilaterian
505 common ancestor. *EvoDevo* **10**, 27 (2019).
506 32. Thiel, D. *et al.* Large-scale deorphanization of Nematostella vectensis neuropeptide
507 G protein-coupled receptors supports the independent expansion of bilaterian and
508 cnidarian peptidergic systems. *eLife* **12**, RP90674 (2024).
509 33. Knabl, P., Mörsdorf, D. & Genikhovich, G. A whole-body atlas of BMP signaling
510 activity in an adult sea anemone. *BMC Biol.* **23**, 49 (2025).
511 34. Marlow, H., Matus, D. Q. & Martindale, M. Q. Ectopic activation of the canonical wnt
512 signaling pathway affects ectodermal patterning along the primary axis during larval
513 development in the anthozoan Nematostella vectensis. *Dev. Biol.* **380**, 324–334
514 (2013).
515 35. Matus, D. Q., Magie, C. R., Pang, K., Martindale, M. Q. & Thomsen, G. H. The
516 Hedgehog gene family of the cnidarian, Nematostella vectensis, and implications for
517 understanding metazoan Hedgehog pathway evolution. *Dev. Biol.* **313**, 501–518
518 (2008).
519 36. Ikmi, A. *et al.* Feeding-dependent tentacle development in the sea anemone
520 Nematostella vectensis. *Nat. Commun.* **11**, 4399 (2020).

37. Ikmi, A. & Gibson, M. C. Identification and In Vivo Characterization of NvFP-7R, a Developmentally Regulated Red Fluorescent Protein of Nematostella vectensis. *PLoS ONE* **5**, e11807 (2010).
38. Leyva-Díaz, E., Masoudi, N., Serrano-Saiz, E., Glenwinkel, L. & Hobert, O. Brn3/POU-IV-type POU homeobox genes—Paradigmatic regulators of neuronal identity across phylogeny. *WIREs Dev. Biol.* **9**, (2020).
39. Simeone, A. *et al.* Orthopedia, a novel homeobox-containing gene expressed in the developing CNS of both mouse and drosophila. *Neuron* **13**, 83–101 (1994).
40. Steinmetz, P. R. *et al.* Six3 demarcates the anterior-most developing brain region in bilaterian animals. *EvoDevo* **1**, (2010).
41. Owens, D. F. & Kriegstein, A. R. Is there more to gaba than synaptic inhibition? *Nat. Rev. Neurosci.* **3**, 715–727 (2002).
42. Sequeira, A., Shen, K., Gottlieb, A. & Limon, A. Human brain transcriptome analysis finds region- and subject-specific expression signatures of GABAAR subunits. *Commun. Biol.* **2**, 153 (2019).
43. Gründer, S. Functional analysis of ligand-gated chloride channels in a cnidarian sheds light on the evolution of inhibitory signalling. (2025).
44. Oren, M., Brikner, I., Appelbaum, L. & Levy, O. Fast Neurotransmission Related Genes Are Expressed in Non Nervous Endoderm in the Sea Anemone Nematostella vectensis. *PLoS ONE* **9**, e93832 (2014).
45. Levy, S. *et al.* Ectopic activation of GABAB receptors inhibits neurogenesis and metamorphosis in the cnidarian Nematostella vectensis. *Nat. Ecol. Evol.* **5**, 111–121 (2020).
46. Koizumi, O. *et al.* The nerve ring in cnidarians: its presence and structure in hydrozoan medusae. *Zoology* **118**, 79–88 (2015).
47. Nielsen, S. K. D., Koch, T. L., Wiisbye, S. H., Grimmelikhuijzen, C. J. P. & Garm, A. Neuropeptide expression in the box jellyfish *Tripedalia cystophora* —New insights into the complexity of a “simple” nervous system. *J. Comp. Neurol.* **529**, 2865–2882 (2021).

551 **Methods**

552

553 **Animals and husbandry**

554 *Nematostella vectensis* anemones were maintained in 12 parts per thousand (ppt)
555 artificial seawater (ASW, Instant Ocean) in glass containers at room temperature (RT,
556 ~22 °C) under low ambient light. Animals were fed freshly hatched *Artemia* nauplii 2–3
557 times per week, and seawater was replaced the following day to remove residual food
558 and waste. Juvenile polyps were raised at 27 °C after their first feeding until sexual
559 maturity, after which adults were kept long-term at either RT or 16 °C as needed. Mixed-
560 sex populations were housed at the Stowers Institute and were originally derived from
561 founder stock provided by Mark Martindale. Unless otherwise specified, all animals
562 used in this study were kept under these standard conditions.

563

564 **Spawning and embryo preparation**

565 Spawning was induced following established *Nematostella* protocols[48,49]. Sexually
566 mature adults were kept at 16 °C, then transferred to RT and placed in front of a light
567 box overnight to induce gamete release. The following morning, dishes were cold-
568 shocked by replacing the water with 16–18 °C 12 ppt ASW. Unfertilized egg sacs were
569 collected for microinjection. Egg sacs were dejellied in 4% L-cysteine prepared in 12 ppt
570 ASW and incubated for 10 min on a gentle rocker. Wide-bore transfer pipettes were
571 used to minimize mechanical damage. Dejellied eggs were washed several times in
572 ASW, transferred to clean dishes, and kept at 16 °C until microinjection or fertilization.

573

574 Fertilized embryos used for fluorescent in situ hybridization and developmental imaging
575 were cultured at 24 °C in the dark under standard conditions. Developmental stages
576 used in this study included planula larvae (3 days post-fertilization, dpf) and primary
577 polyps (7–10 dpf). Primary polyps corresponded to the first sessile feeding stage and
578 were unfed, four-tentacle animals within this early post-metamorphic window. Juveniles
579 were staged by tentacle number. Adults were considered as sexually mature polyps,
580 typically bearing 16 tentacles and older than three months.

581

582 **Transgenic line generation**

583 The *NvSH3GL3*^{P}*>mScarlet-I* reporter construct was designed using a 1.9 kb promoter
584 fragment upstream of the *NvSH3GL3* locus to drive an *mScarlet-I–CAAX–P2A–HaloTag*
585 reporter cassette followed by an SV40 polyadenylation signal. mScarlet-I fluorescence
586 was used for all anatomical imaging. The vector was assembled using the NEBuilder
587 HiFi DNA Assembly Master Mix (NEB, E2621) and sequence-verified prior to injection.
588 Oligonucleotides used for promoter cloning are listed in Supplementary Table 6.
589
590 Unfertilized oocytes were microinjected following established Meganuclease (I-SceI)-
591 mediated transgenesis procedures[21,50]. Injection mix consisted of 10× I-SceI buffer (10
592 mM Tris-HCl, 10 mM $MgCl_2$, 1 mM DTT, pH 8.8), ~50 ng μl^{-1} plasmid DNA, 0.4 U μl^{-1} I-
593 SceI enzyme (NEB, R0694), and FITC (Fisher Scientific, 46425) to visualize injection
594 boluses. The mixture was assembled and pre-incubated according to standard
595 protocol[21]. Microinjection was performed using an Eppendorf FemtoJet, and injected
596 oocytes were fertilized after the injection session (≤ 1 h). Embryos were kept at 18 °C
597 overnight and subsequently raised at RT with regular ASW changes until first feeding.
598
599 Injected animals retaining mosaic reporter expression after two feedings were pooled
600 and raised to adulthood. Individual F0 adults were crossed to wild-type (WT) animals to
601 assess germline transmission. A single F0 female carrier was identified and used to
602 establish the line. Reporter-positive F1 offspring were outcrossed to WT animals,
603 yielding ~50% reporter-positive F2 progeny maintained as a stable heterozygous
604 population. F2 reporter animals were used for all anatomical imaging and single-cell
605 applications. F3 animals were generated by intercrossing F2 individuals, and
606 homozygotes were identified by test-crossing to WT animals, which yielded 100%
607 reporter-positive progeny. Homozygous F3 animals were maintained as genetic stock.
608
609 For anatomical reference in selected live-imaging experiments, a previously generated
610 transgenic reporter expressing GFP under the control of the myosin heavy chain
611 promoter[51] was used to visualize muscle tissue. This reporter was used only for
612 qualitative anatomical comparison and was not employed for quantitative analyses.

613

614 **CRISPR/Cas9 mutant generation**

615 CRISPR/Cas9 genome editing was performed as previously described[20,52]. A single
616 guide RNA (sgRNA) targeting the *NvGABAAR1* coding sequence was designed using
617 the CRISPRscan server[53] (https://www.crisprscan.org/sequence/) with default
618 parameters (Cas9 - NGG, In vitro T7 promoter). The selected sgRNA targeted a site
619 within the ligand-binding domain. A double-stranded DNA template for sgRNA synthesis
620 was generated by annealing the gene-specific forward primer to a universal reverse
621 primer, followed by Klenow extension (37 °C for 30 min, 75 °C for 15 min; Klenow
622 Fragment, NEB, M0210). In vitro transcription was performed using the AmpliScribe T7-
623 Flash Transcription Kit (Biosearch Technologies, ASF250) at 37 °C for 5 h, followed by
624 DNase I treatment for 15 min. The sgRNA was purified using the Direct-zol RNA
625 MiniPrep Kit (Zymo Research, R2052) according to the manufacturer's instructions and
626 quantified using a NanoDrop spectrophotometer (Thermo Fisher Scientific).

627

628 For microinjections, Cas9 protein with NLS (PNA Bio, CP02) was mixed with sgRNA at
629 equal concentrations and diluted to 500 ng μl^{-1} each in nuclease-free water. FITC
630 (Fisher Scientific, 46425) was added to visualize injection boluses. Unfertilized oocytes
631 were injected with Cas9–sgRNA complexes, fertilized with WT sperm following the
632 injection session, and raised at RT.

633

634 To evaluate editing efficiency and identify potential founders, a subset of injected
635 embryos was sacrificed at 3–10 dpf for genotyping, since their small size precludes non-
636 lethal tissue sampling. The remaining injected siblings were raised to adulthood as
637 candidate F0 animals. A single F0 male was identified as carrying a +27 bp insertion,
638 resulting in an premature stop codon within the ligand-binding domain of *NvGABAAR1*.
639 This F0 male was crossed to a homozygous F3 *NvSH3GL3*^{P}*>mScarlet-I* reporter
640 female, and genotyping of 3–10 dpf F1 offspring confirmed germline transmission of the
641 +27 allele. The remaining F1 siblings were raised to juvenile stages and individually
642 genotyped to identify heterozygous *NvGABAAR1*$^{+/+27}$, reporter-positive individuals. All
643 such F1 animals were pooled and intercrossed to generate the F2 generation.

644

645 Individual F2 animals were genotyped to distinguish reporter-positive WT
646 (*NvGABAAR1*$^{+/+}$), heterozygous (*NvGABAAR1*$^{+/+27}$), and homozygous
647 (*NvGABAAR1*$^{+27/+27}$) siblings. F3 WT controls were generated by intercrossing reporter-
648 positive F2 WT siblings (*NvGABAAR1*$^{+/+}$ × *NvGABAAR1*$^{+/+}$), and F3 homozygous
649 mutants were generated by intercrossing reporter-positive F2 homozygous siblings
650 (*NvGABAAR1*$^{+27/+27}$ × *NvGABAAR1*$^{+27/+27}$). All neural-morphology imaging and
651 behavioral assays were conducted on F3 homozygous mutants together with their F3
652 WT siblings. Throughout, "wild-type" refers to same-generation siblings lacking the +27
653 allele rather than unrelated WT animals.
654

655 For genotyping, whole embryos (<10 dpf) or aboral tissue from juveniles and adults was
656 lysed in QuickExtract DNA Extraction Solution (Biosearch Technologies, QE09050) at
657 65 °C for 30 min and 98 °C for 2 min. The *NvGABAAR1* target locus was amplified by
658 PCR, followed by a second round of amplification to introduce sample-specific dual
659 barcodes. Amplicons were pooled and size-selected using the ProNex Size-Selective
660 Purification System (Promega), quantified on a Qubit Fluorometer (Thermo Fisher
661 Scientific), and assessed for size and purity on an Agilent Bioanalyzer. Purified pools
662 were sequenced on an Illumina MiSeq 2 × 250 bp flow cell. The resulting sequence data
663 were demultiplexed, read pairs were joined, and indel frequencies and allele identities
664 were analyzed using CRIS.py[54].
665

666 All primers used for sgRNA template generation and genotyping are listed in
667 Supplementary Table 6.
668

669 **Behavioral assays**

670 *Animal preparation*

671 Adult F3 *NvGABAAR1*$^{+27/+27}$ mutants and their WT siblings were used for all behavioral
672 experiments. Animals were ~1 year post-fertilization and of comparable size; unusually
673 large or small individuals were excluded. Because *Nematostella* lacks reliable external

674 sex markers and no sex-specific differences in feeding behavior are known, mixed-sex
675 animals were used.
676
677 Mutant and WT groups were maintained separately at RT in Pyrex glass dishes under
678 low ambient light, as described above, and kept on the same shelf to minimize
679 environmental variation. Animals were fed freshly hatched *Artemia* once per week. To
680 avoid physiological effects of high-protein or non-native food sources (such as egg
681 white), feeding assays were spaced by at least 4 weeks of routine *Artemia* feeding.
682
683 For each experiment, individual animals were transferred 2–4 days before the assay
684 into sterile 60 × 15 mm polystyrene dishes (Falcon 351007) containing 12 ppt ASW and
685 allowed to acclimate to the brighter ambient illumination near the imaging setup.
686 Seawater was replaced the night before or morning of the assay to remove gametes
687 and metabolic waste. On the day of testing, dishes were placed next to the imaging
688 setup for ≥1 h so animals could fully relax and extend under the recording illumination,
689 which was essential to prevent retraction during dish handling and the assay.
690
691 Animals were assayed 7, 11, or 14 days after their last *Artemia* feeding, with 14-day
692 animals representing the more strongly starved condition. Mutant and WT animals from
693 the same cohort were always tested in parallel on the same day, and datasets pooled
694 measurements across multiple independent assay days.
695
696 *Food preparation*
697 For qualitative behavioral observations, *Artemia* nauplii were used for naturalistic
698 feeding (Supplementary Video 1), whereas mussel tissue, torn into small pieces with
699 fine forceps, was used for assays involving multiple food items, lateral presentation, and
700 sequential feeding (Supplementary Videos 3–5).
701
702 For assays involving standardized food geometry, cylindrical egg-white pellets were
703 prepared from the white portion of hard-boiled chicken eggs (Supplementary Videos 2
704 and 6). Egg-white slices (5–8 mm thick) were cored using an EMS Core Sampling Tool

705 (EMS 69039) and gently pressed into a soft substrate to avoid compression artifacts,
706 generating cylindrical logs. Logs were then cut into pellets with height equal to diameter
707 using a 0.125-mm ultra-fine tungsten dissecting needle (Roboz Surgical RS-6063).
708 Pellets of 0.5, 0.75, 1.0, 1.2, 1.5, and 2.0 mm diameter were used for size-series
709 comparisons (Supplementary Video 2). A diameter of 1.0 mm was selected for all
710 quantitative assays (Supplementary Video 6), as smaller pellets were difficult to track
711 and did not reliably elicit mouth opening, whereas larger pellets introduced variability
712 due to prolonged and inconsistent transit through the pharynx.
713
714 *Food delivery*
715 Food pellets were delivered by either a pipette- or whisker-based approach. In the
716 pipette method, a pellet was released from a glass Pasteur pipette positioned adjacent
717 to a tentacle near the oral opening. Glass pipettes were required because plastic
718 pipettes caused egg-white pellets to adhere to the inner surface and impeded reliable
719 release. This method produced a slight water disturbance, providing both mechanical
720 and chemical cues. In the whisker method, the pellet was first released distally in the
721 dish and then gently guided toward the oral opening using a trimmed cat whisker affixed
722 to a wooden toothpick. The whisker provided sufficient rigidity for precise manipulation
723 while introducing minimal mechanical stimulation. This method enabled more consistent
724 placement of the food stimulus, although grasping onset was typically slower and more
725 variable due to reduced mechanical cues relative to pipette delivery.
726
727 For swallowing analyses, pipette- and whisker-delivered trials were pooled because the
728 delivery method did not significantly affect swallowing durations within each genotype.
729 This was confirmed by the linear mixed-effects models (see Supplementary Table 5).
730 Parallel to these findings, while delivery method influenced grasping durations, the
731 effect was comparable across genotypes (Extended Data Fig. 5f).
732
733 *Feeding assay*
734 Dishes containing single acclimated animals were arranged beside the imaging setup
735 and moved into view with minimal disturbance. All assays were recorded. Food pellets

were delivered by either the pipette or whisker method, as described above. After a pellet was grasped and swallowed, the next trial began only once the ingested pellet had fully passed through the pharynx into the gastrovascular cavity and no further downward movement was observed.

A trial was defined as one pellet presentation and the resulting grasping and swallowing sequence. Each behavioral session (one animal per session) consisted of 4–10 sequential trials, but only the first four consecutive trials (trials 1–4) were used for quantitative analyses. Grasping and swallowing latencies showed no systematic change after the first three trials, and additional trials increased the likelihood of movement artifacts or handling disturbances.

Sessions were excluded if swallowing was accompanied by pronounced bending of the oral region, which mechanically altered ingestion dynamics. Such bending was typically triggered when a centrally delivered pellet was captured by a peripheral tentacle. To avoid these artifacts, any peripheral capture within trials 1–4 led to exclusion of the session. Peripheral capture occurring only after trial 4 did not affect inclusion, as later trials were not analyzed. Sessions were also terminated if the animal retracted into its body column during the assay, even if it later re-extended. Animals with unusually narrow pharynges were excluded to prevent anatomical constraints from influencing timing measurements.

Video acquisition

Behavioral sessions were recorded on a Leica M165 FC stereo microscope equipped with a Flexacam C1 camera. Videos were acquired at 1× magnification and 0.73× zoom, at either 0.50 or 0.87 s/frame.

Behavior annotation

Grasping and swallowing were quantified from time-lapse recordings as two sequential phases of the feeding response. For quantification, grasping was defined as the period from the first tentacle-driven engagement of the pellet to the onset of neck constriction,

767 and swallowing as the period from the initiation of neck constriction to the moment the
768 pellet reached the distal end of the pharynx.
769
770 For each trial, three frames were manually identified in Fiji:
771 t1 — first clear grasping movement after pellet introduction, marked by the onset of a
772 tentacle-driven pull toward the mouth.
773 t2 — beginning of neck constriction, often coinciding with or following a tentacle
774 clasping motion.
775 t3 — frame in which the pellet reached the distal end of the pharynx. This endpoint was
776 used because the time from this point to entry into the gastrovascular cavity varied
777 widely across trials and individuals.
778
779 Grasping and swallowing durations were calculated as the frame difference multiplied
780 by the corresponding seconds-per-frame value: $T_{grasp} = (t2 - t1) \times$ s/frame and
781 $T_{swallow} = (t3 - t2) \times$ s/frame. Frame numbers and timestamps were recorded in Excel
782 for downstream analysis.
783
784 *Visualization and statistics*
785 Data processing and visualization were performed in R (v4.4.1) using ggplot2 (v3.5.2)
786 and standard tidyverse packages. Individual trial trajectories were plotted as faint lines,
787 and genotype-wise mean ± s.e.m. were overlaid as solid lines. Grasping plots included
788 pipette-delivery trials only, whereas swallowing plots included both pipette- and whisker-
789 delivery methods.
790
791 All statistical analyses were performed in R. All statistical tests were two-sided. Feeding
792 durations were analyzed using linear mixed-effects models fitted with lme4[55] (v1.1-38).
793 AnimalID was included as a random intercept to account for repeated measurements
794 from the same individual across trials. Fixed effects included genotype and trial number.
795 For swallowing analyses, food delivery method and starvation duration were included as
796 additional covariates.
797

798 Significance of main effects and interactions was assessed using Type III Analysis of
799 Variance (ANOVA) with Satterthwaite's method implemented in lmerTest[56] (v3.1-3).
800 Genotype differences at each trial were estimated using estimated marginal means and
801 pairwise contrasts computed with emmeans[57] (v2.0.0), utilizing the Kenward-Roger
802 approximation for degrees of freedom. The resulting estimates, standard errors,
803 confidence intervals, and p-values are provided in Supplementary Table 5. Statistical
804 inference relied on the assumptions of linear mixed-effects models; no additional tests
805 of normality or global multiple-comparison corrections were performed.
806
807 **Whole-mount staining**
808 Whole-mount staining was performed following previously published protocols[58] for
809 *Nematostella* with minor modifications. Planula larvae (3 dpf) and primary polyps (7–10
810 dpf) were collected into 1 ml ASW in round-bottom tubes. Primary polyps were allowed
811 to relax for ≥ 15 min, after which $MgCl_2$ was added stepwise by adding 100 µl of 7%
812 $MgCl_2$ in 12 ppt ASW, incubating for 5 min, and repeating once more. Planula larvae
813 were immobilized by adding 7% $MgCl_2$ directly, without a relaxation period. After
814 immobilization, the solution was removed and replaced with fixative.
815
816 For visualization of F-actin in fixed transgenic reporter animals, samples were fixed in
817 4% paraformaldehyde (PFA) in 12 ppt ASW for 1 h at RT with gentle rocking, followed
818 by washing 5 × 5 min in phosphate-buffered saline (PBS) containing 0.1% Tween-20
819 (PBTw). Samples were then incubated overnight at 4 °C on a shaker with either Alexa
820 Fluor 488-conjugated phalloidin (1:300) or SiR-actin (Cytoskeleton, CY-SC001; 1:1000),
821 washed again in PBTw, and cleared by immersion in ScaleA2 (2 M urea, 75% glycerol
822 in water) prior to mounting and imaging.
823
824 For GABA immunostaining, animals were fixed for 3 min in 4% PFA supplemented with
825 0.05% glutaraldehyde in 12 ppt ASW, followed by post-fixation in 4% PFA in 12 ppt
826 ASW for 1 h at room temperature with gentle rocking. Samples were washed 5 × 5 min
827 in PBTw and incubated in blocking buffer (PBTw supplemented with 5% normal goat
828 serum, 1% bovine serum albumin, and 10% dimethyl sulfoxide [DMSO]) for 2 h at RT.

829 Primary antibody incubation was performed overnight at 4 °C on a shaker using rabbit
830 anti-GABA (Sigma-Aldrich, A2052; 1:500) diluted in blocking buffer without DMSO. The
831 following day, samples were washed 6 × 20 min in PBTw and incubated overnight at
832 4 °C on a shaker with goat anti-rabbit Alexa Fluor 647 secondary antibody (Invitrogen,
833 A-21245; 1:1000) diluted in blocking buffer without DMSO. Samples were then washed
834 6 × 20 min in PBTw and cleared in ScaleA2 prior to imaging.
835
836 **Whole-mount fluorescent in situ hybridization**
837 Gene-specific probe regions were selected and verified for specificity by BLAST
838 searches against the *Nematostella* transcriptome. Nested PCR on cDNA templates
839 amplified the target region, and the second-round reverse primer incorporated a T7
840 promoter sequence for in vitro transcription. Final PCR products were Sanger-
841 sequenced to confirm identity. DIG-labeled antisense RNA probes were generated by in
842 vitro transcription using the DIG RNA Labeling Mix (Roche, 11277073910), followed by
843 DNase I treatment and column purification (Zymo Research, R2052). Primer sequences
844 used for probe generation are listed in Supplementary Table 6.
845
846 FISH was performed based on established *Nematostella* protocols[59]. In brief, animals
847 were immobilized as described for immunostaining, pre-fixed for 90 s in ice-cold 4%
848 PFA + 2.5% glutaraldehyde in 12 ppt ASW, and then fixed in 4% PFA in 12 ppt ASW for
849 1 h at RT. Samples were washed in PBS and dehydrated through a PBS/methanol
850 series into 100% methanol. Endogenous peroxidase activity was quenched in 3% H_2O_2
851 in 90% methanol for 1 h at RT, followed by rehydration through a methanol/PBS series.
852 Tissues were permeabilized with Proteinase K (20 µg ml^{-1} for 10 min), post-fixed in 4%
853 PFA for 1 h, washed in PBTw, and transitioned into hybridization buffer at 60 °C, where
854 they were pre-hybridized overnight. DIG-labeled probes (1 ng $µl^{-1}$) were denatured at
855 80 °C for 10 min, snap-cooled on ice, and hybridized to samples at 60 °C for 48 h. After
856 hybridization, samples were washed at 60 °C through SSC solutions of increasing
857 stringency, then returned to RT and washed into TNT (0.1 M Tris-HCl pH 7.5, 0.15 M
858 NaCl, 0.1% Tween-20). Samples were blocked in TNT containing 5% sheep serum and
859 1% blocking reagent (Roche) for 2 h at RT, then incubated overnight at 4 °C with anti-

860 DIG-POD Fab fragments (Roche, 11207733910; 1:1000). Fluorescent signal was
861 developed using the TSA Cyanine 3 system (Akoya, NEL704A001KT) for 20 min at RT.
862 After washing into PBTw, samples were counterstained with SiR-DNA (Cytoskeleton,
863 CY-SC007; 1:1000), cleared in ScaleA2, and mounted for imaging as described for
864 immunostaining.
865
866 **Imaging and image processing**
867 All samples were imaged on either a Nikon spinning-disk confocal system (20× or 40×
868 objectives) or an Andor Dragonfly spinning-disk confocal microscope (25× or 40×
869 objectives). Z-stacks were acquired at 1-µm step size. Maximum intensity projections,
870 orthogonal views generated by reslicing, and all subsequent image processing (rotation,
871 cropping, and linear min/max intensity scaling) were performed in Fiji for visualization.
872
873 **Single-cell RNA-seq**
874 *Tissue dissociation and cell sorting*
875 Adult F2 *NvSH3GL3*^{P}*>mScarlet-I* animals were used for the single-cell RNA-seq
876 experiment. All animals were of mixed sex, and the workflow was performed as a single
877 batch on the same day. Animals were fasted for five days and transferred from 16 °C to
878 RT for ~8 h before dissociation. Animals were kept in 12 ppt ASW until fully relaxed and
879 immobilized by gradually adding a 7% $MgCl_2$ solution prepared in ASW (Sigma-Aldrich,
880 M2670). Oral discs were dissected by a single transverse cut just below the pharynx,
881 with most tentacles trimmed away. Dissected tissues were briefly rinsed in Ca^{2+}/Mg^{2+}-
882 free ASW (154 mM NaCl, 3.57 mM KCl, 0.70 mM $NaHCO_3$, 2.33 mM Na_2SO_4; all salts
883 from Sigma-Aldrich), then briefly ground (~15 s) and gently triturated for ~20 min at RT
884 in Ca^{2+}/Mg^{2+}-free ASW containing L-cysteine (2 mg ml^{-1}; Sigma-Aldrich, 168149),
885 papain (4 mg ml^{-1}; Sigma-Aldrich, P4762), and Liberase TM (0.05 mg ml^{-1}; Roche,
886 5401119001). Cell suspensions were filtered through 30 µm filters (FILCONS 030-33s;
887 CTSV), pelleted (300 × g, 10 min, 4 °C), washed in enzyme-free Ca^{2+}/Mg^{2+}-free ASW,
888 and stained on ice for 5 min with DAPI (2 µg ml^{-1}; Sigma-Aldrich, D9542) and DRAQ5
889 (25 µM; Thermo Fisher Scientific, 62251).
890

891 Cells were analyzed and sorted on a BD Influx flow cytometer (100 µm nozzle, 20 psi).
892 Excitation and emission were collected for DAPI (345/455 nm), DRAQ5 (647/697 nm),
893 and mScarlet-I (578/613 nm). Because *Nematostella* oral tissue exhibits strong
894 autofluorescence from the endogenous red fluorescent protein NvFP-7R[37] (569/593
895 nm), gating was anchored using a fluorescence-minus-one (FMO) control prepared from
896 WT oral-disc cells stained with DAPI and DRAQ5 but lacking mScarlet-I. This control
897 captured the autofluorescence range of NvFP-7R and defined the background threshold
898 for the reporter channel. A tentacle sample expressing mScarlet-I but lacking NvFP-7R
899 established the mScarlet-I emission profile. Reporter-positive gates retained events
900 bright in the mScarlet-I detector and dim in an adjacent 670/30 channel, minimizing
901 NvFP-7R carryover. Only singlets and live, nucleated events ($DAPI^-/DRAQ5^+$) were
902 included. The final gate contained ~2% of total events in the reporter population versus
903 0.1% in the FMO control, yielding approximately 45,700 sorted events collected into
904 RNase-free tubes for single-cell RNA-seq.
905
906 *Library preparation and sequencing*
907 Dissociated and sorted cells were assessed for concentration and viability using a
908 LUNA-FL Cell Counter (Logos Biosystems). Samples with ≥ 90% viable cells were
909 loaded onto a Chromium Controller (10x Genomics), targeting recovery of ~3,200 cells.
910 Single-cell cDNA libraries were prepared with the Chromium Single Cell 3′ Reagent Kit
911 v3 (10x Genomics) according to the manufacturer's instructions. cDNA and final short-
912 fragment libraries were evaluated for quality and quantity using a 2100 Bioanalyzer
913 (Agilent Technologies) and a Qubit Fluorometer (Thermo Fisher Scientific). Libraries
914 were sequenced on an Illumina NextSeq 500 to a mean depth of ≥ 100,000 reads per
915 cell (paired-end 28 × 8 × 91 bp) using Real-Time Analysis (RTA) and instrument
916 software versions current at the time of sequencing.
917
918 FASTQ files were processed with Cell Ranger (v8.0.1; 10x Genomics,
919 https://www.10xgenomics.com/) against the *Nematostella vectensis* genome assembly
920 jaNemVect1.1 (GCF_932526225.1; NCBI RefSeq[60] Annotation Release 101),
921 supplemented with the *NvSH3GL3^P>mScarlet-I* reporter sequence. The resulting gene–

922 cell count matrix was analyzed in Seurat[61] (v5.1.0) in R (v4.4.1). Cells were retained if
923 they expressed 200–3,000 genes, contained ≤ 15,000 unique molecular identifiers
924 (UMIs), and exhibited < 5% mitochondrial gene content (identified from RefSeq-
925 annotated mitochondrial gene prefixes). Data were normalized with SCTransform[62], and
926 the top 3,000 most variable genes were used for principal-component analysis (PCA).
927 The first 15 principal components were used to construct a shared nearest-neighbor
928 graph (FindNeighbors) and perform graph-based clustering (FindClusters, resolution =
929 0.5). Uniform Manifold Approximation and Projection (UMAP) embeddings computed
930 from the same components were used for visualization.
931
932 *Clustering and analysis*
933 Cluster identities were assigned by examining marker genes identified with
934 FindAllMarkers and cross-referenced with manually curated *Nematostella* gene sets for
935 neuronal developmental, synaptic function, sensory transduction and neurotransmitter
936 receptors (Supplementary Tables 1 and 2). These curated lists were generated from
937 NCBI RefSeq annotations using keyword-based filtering and provided the framework for
938 assigning biologically meaningful identities to each cluster.
939
940 Gene-set quantification was performed using the same manually curated gene lists.
941 Expression was evaluated from the SCT-normalized count layer, and a gene was
942 considered detected in a cluster if it exhibited non-zero expression and was expressed
943 in more than 10% of cells in that cluster. For each gene set, per-cluster counts of
944 detected genes and per-gene summary tables (average expression, percent of
945 expressing cells, and annotation metadata) are provided in Supplementary Table 2.
946
947 All visualizations were generated in R using Seurat (v5.1.0), ggplot2 (v3.5.2), ggtern
948 (v3.5.0), pheatmap (v1.0.12), patchwork (v1.3.0), and standard tidyverse packages. All
949 analysis and visualization code is available at [link].
950
951 **Bulk RNA-seq**

952 Adult male *Nematostella vectensis* polyps (n = 3 individuals) were dissected into four
953 tissue types (pharynx, body wall, proximal tentacles, and oral disc), yielding twelve total
954 samples (three biological replicates per tissue). Each tissue piece was immersed in 300
955 µl TRIzol reagent (Invitrogen, 15596026) and snap-frozen in liquid nitrogen before
956 storage at –80 °C. RNA was extracted using the Direct-zol RNA MiniPrep Kit (Zymo
957 Research, R2052) following the manufacturer's protocol, including a 15 min on-column
958 DNase I digestion to remove genomic DNA.
959
960 mRNA-seq libraries were generated from 100 ng (or < 100 ng for two samples) of high-
961 quality total RNA, as assessed using the Bioanalyzer (Agilent). Libraries were prepared
962 using the TruSeq Stranded mRNA Library Prep Kit (Illumina, 20020594) and TruSeq
963 RNA Single Indexes Sets A and B (Illumina, 20020492 and 20020493). Libraries were
964 purified using the AMPure XP bead-based reagent (Beckman Coulter, A63882),
965 evaluated for quality and quantity using the Bioanalyzer (Agilent) and Qubit Fluorometer
966 (Life Technologies). Equal-molar libraries were pooled, quantified, and sequenced as 75
967 bp paired-end reads on a mid-output flow cell using the NextSeq 500 (Illumina).
968 Following sequencing, demultiplexing and FASTQ generation were performed using
969 Illumina RTA (v2.4.11) and bcl2fastq2 (v2.20).
970
971 FASTQ files were aligned to the *Nematostella vectensis* genome assembly
972 jaNemVect1.1 (GCF_932526225.1; NCBI RefSeq[60] Annotation Release 101) using
973 STAR[63] (v2.7.10b) with quantMode GeneCounts to obtain gene-level counts. Alignment
974 summary rows were removed and raw counts were imported into R and analyzed with
975 edgeR[64] (v4.2.2). Lowly expressed genes were filtered using filterByExpr with tissue as
976 the grouping factor, and library sizes were normalized using the trimmed mean of M-
977 values (TMM) method. Gene lengths were obtained from the corresponding RefSeq
978 gene models and used to compute TPM values from the filtered count matrix. For
979 visualization, TPM values were averaged across biological replicates for each tissue,
980 restricted to a curated list of GABA receptor-like subunits (Supplementary Table 3), and
981 scaled per gene (row-wise) before generating clustered heatmaps.
982

983 **Phylogenetic analysis**

984 *Sequence identification and curation*

985 Putative *Nematostella vectensis* γ-aminobutyric acid type A receptor ($GABA_AR$) and
986 glycine receptor (GlyR) subunits were first identified by BLASTp[65] searches (v2.13.0+)
987 against the *Homo sapiens* $GABA_AR$ and GlyR sequences and verified for domain
988 composition using the InterPro server[66]. Although orthology between $GABA_AR$ and GlyR
989 types remains unresolved in early-branching metazoans, no hits overlapped with
990 nicotinic acetylcholine, 5-HT_3, or other members of the Cys-loop ligand-gated ion
991 channel (LGIC) superfamily. These sequences are therefore collectively referred to as
992 $GABA_AR$-like subunits throughout.

993

994 For *Nematostella*, candidate $GABA_AR$-like sequences were compiled from three curated
995 sources: the NCBI RefSeq proteome[60,19]
996 (https://www.ncbi.nlm.nih.gov/datasets/genome/GCF_932526225.1/) and two
997 SIMRBase transcriptome-derived proteome assemblies[18] (NV2: wein_nvec200_tcsv2;
998 NVE: wien_nvec200_v1; https://simrbase.stowers.org/starletseaanemone). Not all loci
999 were represented across all datasets. When the same locus appeared in multiple
1000 sources, we retained the longest predicted amino-acid product; when sequences were
1001 equal in length, the RefSeq entry was selected. This procedure yielded 40 curated
1002 *Nematostella* $GABA_AR$-like subunits: 37 for which the RefSeq version was retained, 2
1003 for which RefSeq lacked annotated protein entries and the longest ORFs were
1004 contributed by the NV2 assembly, and 1 for which the longest ORF was contributed by
1005 the NVE assembly, despite orthologous predictions also present in RefSeq and NV2
1006 (Supplementary Table 3).

1007

1008 Homologous $GABA_AR$-like sequences for comparative phylogenetic analysis were
1009 retrieved from UniProt[67] (Swiss-Prot and TrEMBL; downloaded February 2024) for six
1010 bilaterian species (*Homo sapiens*, *Danio rerio*, *Drosophila melanogaster*,
1011 *Caenorhabditis elegans*, *Ciona intestinalis*, and *Octopus vulgaris*). The *Nematostella*
1012 and bilaterian sequences were used as queries for BLASTp[65] searches against six
1013 additional cnidarian proteomes representing both anthozoans (*Acropora millepora*,

1014 *Exaiptasia diaphana*, *Stylophora pistillata*) and medusozoans (*Clytia hemisphaerica,*
1015 *Hydra vulgaris*, *Hydractinia symbiolongicarpus*). Resulting sequences from these
1016 searches were further curated using CD-HIT[68,69] (v4.8.1) to remove redundant
1017 sequences sharing ≥ 90 % similarity within each species. Protein database sources,
1018 accession numbers, and annotations for all taxa are listed in Supplementary Table 4.
1019
1020 *Sequence alignment and phylogeny reconstruction*
1021 The non-redundant candidates from all species were aligned with MAFFT[70] (v7.520)
1022 using the L-INS-i algorithm, and discordant sequences were excluded after manual
1023 inspection. Domain composition was re-evaluated using the InterPro server[66]
1024 (https://www.ebi.ac.uk/interpro/search/sequence/, accessed 19 Nov 2024), and
1025 sequences matching the $GABA_A$R/GlyR α-subunit domain (IPR006028) were retained.
1026 No matches to the GlyR β-subunit domain (IPR008060) were detected. The final
1027 alignment was trimmed with TrimAl[71] (v1.4.rev22) using the -gappyout flag.
1028
1029 A maximum-likelihood phylogeny was constructed using the IQ-TREE 2 server[72]
1030 (v1.6.12; http://iqtree.cibiv.univie.ac.at/, accessed March 2025) under the LG+I+G4
1031 substitution model selected by ModelFinder[73]. Branch support values were estimated
1032 from 1,000 replicates using ultrafast bootstrap (-bb)[74] and SH-like approximate
1033 likelihood-ratio tests (-alrt)[75]. Representative nicotinic acetylcholine receptor (nAChR)
1034 subunits were included as an outgroup to root the tree. The resulting phylogeny was
1035 visualized in FigTree (v1.4.4; http://tree.bio.ed.ac.uk/software/figtree/) and formatted
1036 using Inkscape (v1.3; www.inkscape.org) and Adobe Illustrator (v30.0).
1037
1038 **AlphaFold structure prediction**
1039 The predicted structure of the *Nematostella vectensis* $GABA_A$R-like subunit
1040 NvGABAAR1 was generated using the AlphaFold3 web server[76]
1041 (https://alphafoldserver.com, accessed June 2025), using the longest annotated RefSeq
1042 isoform (gene ID: LOC5505184; protein ID: XP_048587017.1) as input. Predictions
1043 were run with default parameters, and the top-ranked structural model was used for
1044 visualization and structural comparison.

1045

1046 For cross-species comparison, AlphaFold-predicted structures of *Homo sapiens* GABA
1047 type A receptor subunits GABRR3 (UniProt A8MPY1), GABRA2 (UniProt P47869), and
1048 GABRG1 (UniProt Q8N1C3) were obtained from the AlphaFold Protein Structure
1049 Database in July 2025. All human structures correspond to AlphaFold models version
1050 v4 (AF-*-F1-v4).

1051

1052 Structural visualization and pairwise alignment were performed in UCSF ChimeraX[77]
1053 (v1.9). All models were colored by per-residue model confidence, measured as
1054 predicted Local Distance Difference Test (pLDDT), and aligned using the MatchMaker
1055 algorithm.

1056

1057 **Use of AI tools**

1058 Large language models (ChatGPT, OpenAI) were used under author direction to assist
1059 with code generation, debugging, and improving clarity of written text. All scientific
1060 analyses, code execution, and validation were performed by the authors.

1061

1062 **Data availability**

1063 Single-cell RNA-seq and bulk RNA-seq datasets generated in this study have been
1064 deposited in the Gene Expression Omnibus (GEO) under accession numbers
1065 GSE316974 and GSE316975. All source data will be deposited in the Stowers Original
1066 Data Repository (ODR) prior to publication. Additional supporting data are available
1067 from the corresponding author upon request.

1068

1069 **Code availability**

1070 Custom R scripts used for data analysis and figure generation are provided with this
1071 submission and will be made publicly available upon publication.

1072

Methods References

48. Genikhovich, G. & Technau, U. Induction of Spawning in the Starlet Sea Anemone *Nematostella vectensis* , In Vitro Fertilization of Gametes, and Dejellying of Zygotes. *Cold Spring Harb. Protoc.* **2009**, pdb.prot5281 (2009).
49. Stefanik, D. J., Friedman, L. E. & Finnerty, J. R. Collecting, rearing, spawning and inducing regeneration of the starlet sea anemone, Nematostella vectensis. *Nat. Protoc.* **8**, 916–923 (2013).
50. Layden, M. J., Röttinger, E., Wolenski, F. S., Gilmore, T. D. & Martindale, M. Q. Microinjection of mRNA or morpholinos for reverse genetic analysis in the starlet sea anemone, Nematostella vectensis. *Nat. Protoc.* **8**, 924–934 (2013).
51. Renfer, E., Amon-Hassenzahl, A., Steinmetz, P. R. H. & Technau, U. A muscle-specific transgenic reporter line of the sea anemone, *Nematostella vectensis*. *Proc. Natl. Acad. Sci.* **107**, 104–108 (2010).
52. *Whole-Body Regeneration: Methods and Protocols*. vol. 2450 (Springer US, New York, NY, 2022).
53. Moreno-Mateos, M. A. *et al.* CRISPRscan: designing highly efficient sgRNAs for CRISPR-Cas9 targeting in vivo. *Nat. Methods* **12**, 982–988 (2015).
54. Connelly, J. P. & Pruett-Miller, S. M. CRIS.py: A Versatile and High-throughput Analysis Program for CRISPR-based Genome Editing. *Sci. Rep.* **9**, 4194 (2019).
55. Bates, D., Mächler, M., Bolker, B. & Walker, S. Fitting Linear Mixed-Effects Models Using **lme4**. *J. Stat. Softw.* **67**, (2015).
56. Kuznetsova, A., Brockhoff, P. B. & Christensen, R. H. B. **lmerTest** Package: Tests in Linear Mixed Effects Models. *J. Stat. Softw.* **82**, (2017).
57. Lenth, R. V. & Piaskowski, J. emmeans: Estimated Marginal Means, aka Least-Squares Means. (2025).
58. Genikhovich, G. & Technau, U. Anti-acetylated Tubulin Antibody Staining and Phalloidin Staining in the Starlet Sea Anemone *Nematostella vectensis*. *Cold Spring Harb. Protoc.* **2009**, pdb.prot5283 (2009).
59. Steinmetz, P. R. H., Aman, A., Kraus, J. E. M. & Technau, U. Gut-like ectodermal tissue in a sea anemone challenges germ layer homology. *Nat. Ecol. Evol.* **1**, 1535–1542 (2017).

1104 60. Goldfarb, T. *et al.* NCBI RefSeq: reference sequence standards through 25 years of
1105 curation and annotation. *Nucleic Acids Res.* **53**, D243–D257 (2025).
1106 61. Hao, Y. *et al.* Dictionary learning for integrative, multimodal and scalable single-cell
1107 analysis. *Nat. Biotechnol.* **42**, 293–304 (2024).
1108 62. Hafemeister, C. & Satija, R. Normalization and variance stabilization of single-cell
1109 RNA-seq data using regularized negative binomial regression. *Genome Biol.* **20**,
1110 296 (2019).
1111 63. Dobin, A. *et al.* STAR: ultrafast universal RNA-seq aligner. *Bioinformatics* **29**, 15–21
1112 (2013).
1113 64. Robinson, M. D., McCarthy, D. J. & Smyth, G. K. edgeR : a Bioconductor package
1114 for differential expression analysis of digital gene expression data. *Bioinformatics* **26**,
1115 139–140 (2010).
1116 65. Altschul, S. F., Gish, W., Miller, W., Myers, E. W. & Lipman, D. J. Basic local
1117 alignment search tool. *J. Mol. Biol.* **215**, 403–410 (1990).
1118 66. Blum, M. *et al.* InterPro: the protein sequence classification resource in 2025.
1119 *Nucleic Acids Res.* **53**, D444–D456 (2025).
1120 67. The UniProt Consortium *et al.* UniProt: the Universal Protein Knowledgebase in
1121 2025. *Nucleic Acids Res.* **53**, D609–D617 (2025).
1122 68. Li, W. & Godzik, A. Cd-hit: a fast program for clustering and comparing large sets of
1123 protein or nucleotide sequences. *Bioinformatics* **22**, 1658–1659 (2006).
1124 69. Fu, L., Niu, B., Zhu, Z., Wu, S. & Li, W. CD-HIT: accelerated for clustering the next-
1125 generation sequencing data. *Bioinformatics* **28**, 3150–3152 (2012).
1126 70. Katoh, K. & Standley, D. M. MAFFT Multiple Sequence Alignment Software Version
1127 7: Improvements in Performance and Usability. *Mol. Biol. Evol.* **30**, 772–780 (2013).
1128 71. Capella-Gutiérrez, S., Silla-Martínez, J. M. & Gabaldón, T. trimAl: a tool for
1129 automated alignment trimming in large-scale phylogenetic analyses. *Bioinformatics*
1130 **25**, 1972–1973 (2009).
1131 72. Minh, B. Q. *et al.* IQ-TREE 2: New Models and Efficient Methods for Phylogenetic
1132 Inference in the Genomic Era. *Mol. Biol. Evol.* **37**, 1530–1534 (2020).

73. Kalyaanamoorthy, S., Minh, B. Q., Wong, T. K. F., Von Haeseler, A. & Jermiin, L. S. ModelFinder: fast model selection for accurate phylogenetic estimates. *Nat. Methods* **14**, 587–589 (2017).
74. Hoang, D. T., Chernomor, O., Von Haeseler, A., Minh, B. Q. & Vinh, L. S. UFBoot2: Improving the Ultrafast Bootstrap Approximation. *Mol. Biol. Evol.* **35**, 518–522 (2018).
75. Anisimova, M., Gil, M., Dufayard, J.-F., Dessimoz, C. & Gascuel, O. Survey of Branch Support Methods Demonstrates Accuracy, Power, and Robustness of Fast Likelihood-based Approximation Schemes. *Syst. Biol.* **60**, 685–699 (2011).
76. Abramson, J. *et al.* Accurate structure prediction of biomolecular interactions with AlphaFold 3. *Nature* **630**, 493–500 (2024).
77. Meng, E. C. *et al.* UCSF ChimeraX : Tools for structure building and analysis. *Protein Sci.* **32**, e4792 (2023).

Acknowledgements

We thank Boris Rubinstein and Kausik Si for discussions on behavioral experiments, and Kausik Si additionally for advice on neurotransmitter receptor composition analysis. We thank Joshua Zimmerberg for discussions on body size and nerve net scalability, and to Neşet Özel for insights into the relevance of the vesicular GABA transporter in shaping interneuron identity. We are grateful to Mark Miller for creating the *Nematostella* life-cycle illustration, and to past and present members of the Gibson lab for discussions and support. We acknowledge the Stowers Technology Centers for assistance: the Aquatics team for animal husbandry; the Cytometry team, particularly Jillian Blanck, for cell sorting; the Sequencing and Discovery Genomics team for library preparation and sequencing; the Computational Biology team for processing of sequencing data; the Genome Engineering team for CRISPR genotyping; and the Microscopy Center for imaging training and support. This work was supported by the Stowers Institute for Medical Research.

Author contributions

R.Z. conceived and designed the study; performed all experiments and data analyses; prepared the figures; and wrote the manuscript. M.C.G. supervised the research, provided guidance, and edited the manuscript. C.W.S. performed preprocessing of sequencing data, generated genome-assembly mapping tables, and supervised code implementation. A.M.L.K. performed sequence alignment and phylogenetic tree construction. All authors reviewed and approved the final manuscript.

Competing interests

The authors declare no competing interests.

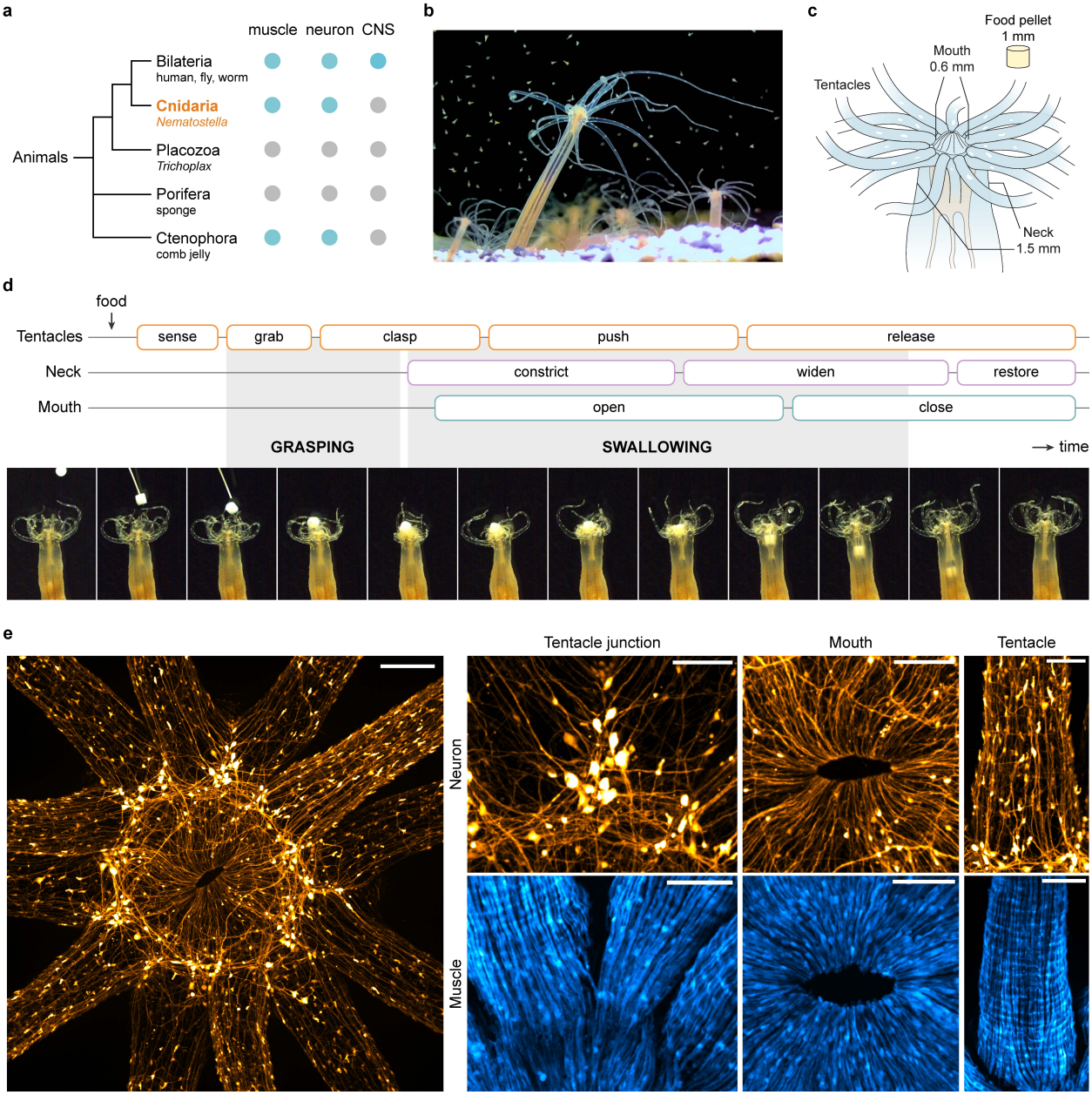

Figure 1 | Structured motor coordination and a ganglion-like oral nerve ring in *Nematostella vectensis*.

(a) Phylogenetic distribution of muscles, neurons, and centralized nervous systems (CNS) across major animal lineages; the dotted branch indicates unresolved phylogenetic relationships. **(b)** Adult *Nematostella vectensis* partially buried in gravel while capturing live brine shrimp (*Artemia*). A corresponding video is provided in Supplementary Video 1. **(c)** Schematic of the standardized feeding paradigm, showing the relative geometry of the oral disc, tentacles, and neck, and the size of the food pellet

1182 (1 mm). **(d)** Time-lapse montage illustrating two sequential phases of feeding, grasping
1183 and swallowing, separated by the onset of neck constriction. Each phase is composed
1184 of coordinated motor subroutines executed by the tentacles, neck, and mouth. A
1185 corresponding time-lapse video is provided in Supplementary Video 6. **(e)** Live confocal
1186 images of juvenile *Nematostella vectensis* expressing the neuronal reporter
1187 *NvSH3GL3*^{P}*>mScarlet-I* (orange) or a muscle reporter driven by the myosin heavy chain
1188 promoter[51] (blue). Neuronal and muscle images were acquired from separate animals
1189 and are shown for anatomical reference. Left, overview of the oral region showing
1190 dense neuronal labeling in the oral disc and tentacles. Right, enlarged views of selected
1191 regions reveal distinct neuronal morphologies and spatial organization. Neurons with
1192 enlarged somata, relative to surrounding neurons, cluster at tentacle junctions and
1193 extend circumferential neurites, forming a ring-like pattern. Additional neurons exhibit
1194 smaller somata and distinct projection orientations, with radial projections around the
1195 oral opening and longitudinal projections within tentacles. Scale bars, 100 μm
1196 (overview) and 50 μm (enlarged views).
1197

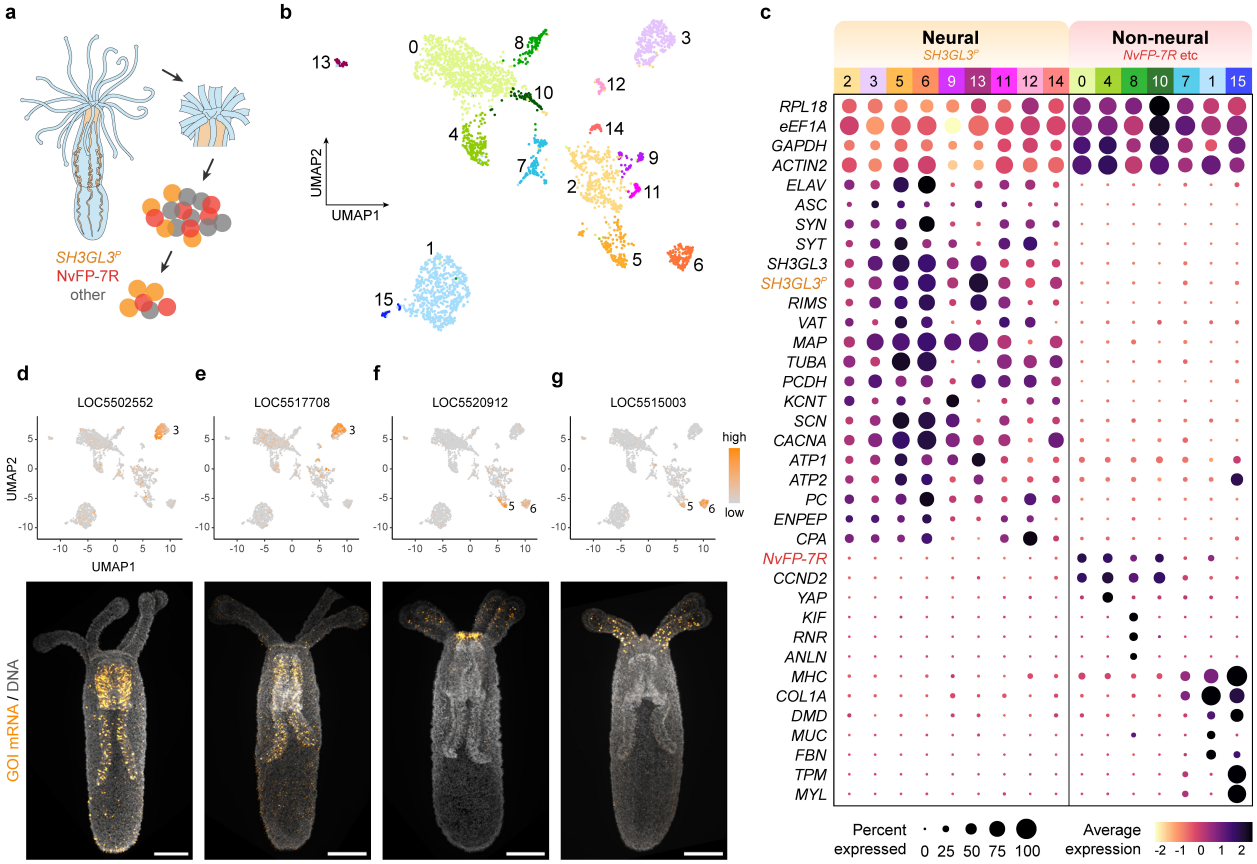

Figure 2 | Molecular diversity and spatial organization of the oral nerve net. **(a)** Schematic of oral-end dissection and cell enrichment for single-cell RNA sequencing. Oral ends from adult *Nematostella vectensis* were dissected and most tentacles trimmed prior to mechanical and enzymatic dissociation for 10x Genomics single-cell RNA sequencing. Cells were enriched for *NvSH3GL3^{P}>mScarlet-I*-positive populations by fluorescence-activated cell sorting (FACS), with gating applied to reduce spectral contamination from cells expressing the native red fluorescent protein NvFP-7R. Colors indicate major cell populations (orange, *NvSH3GL3^{P}>mScarlet-I*; red, NvFP-7R; gray, other). **(b)** UMAP visualization of 3,297 cells from the single-cell dataset. **(c)** Dot plot showing representative gene categories, including housekeeping genes, canonical neuronal and synaptic markers, cytoskeletal components, ion channels and transporters, and adhesion/signaling molecules. Dot size indicates the percentage of cells expressing each gene, and color represents scaled average expression (pale yellow to dark purple). Neural clusters (left) show strong *SH3GL3^{P}* expression, whereas non-neural clusters (right) include *NvFP-7R*-enriched populations as well as clusters

1214 enriched for contractile, cytoskeletal, and extracellular-matrix genes. Expression of the
1215 *SH3GL3*^{P} reporter parallels endogenous *SH3GL3*, supporting reporter fidelity. A
1216 complete list of neural genes with identifiers is provided in Extended Data Fig. 2a. **(d–g)**
1217 Feature plots (top) show SCT-normalized gene expression projected onto the UMAP,
1218 with corresponding fluorescent in situ hybridization (FISH) images (bottom) in four-
1219 tentacle primary polyps (7–10 days post-fertilization, dpf) for four representative cluster-
1220 enriched genes. (d,e) LOC5502552 and LOC5517708 are enriched in cluster 3 and
1221 display predominant expression in the pharyngeal region by FISH. (f,g) LOC5520912
1222 and LOC5515003 are expressed in partially overlapping subsets of clusters 5 and 6 and
1223 show predominant FISH signal in the oral disc and tentacles. Feature plots are scaled
1224 independently for each gene, with light gray indicating no detectable expression and
1225 increasing color intensity indicating higher expression. DNA is shown in gray and gene-
1226 specific signal in orange. Scale bars, 100 μm.
1227

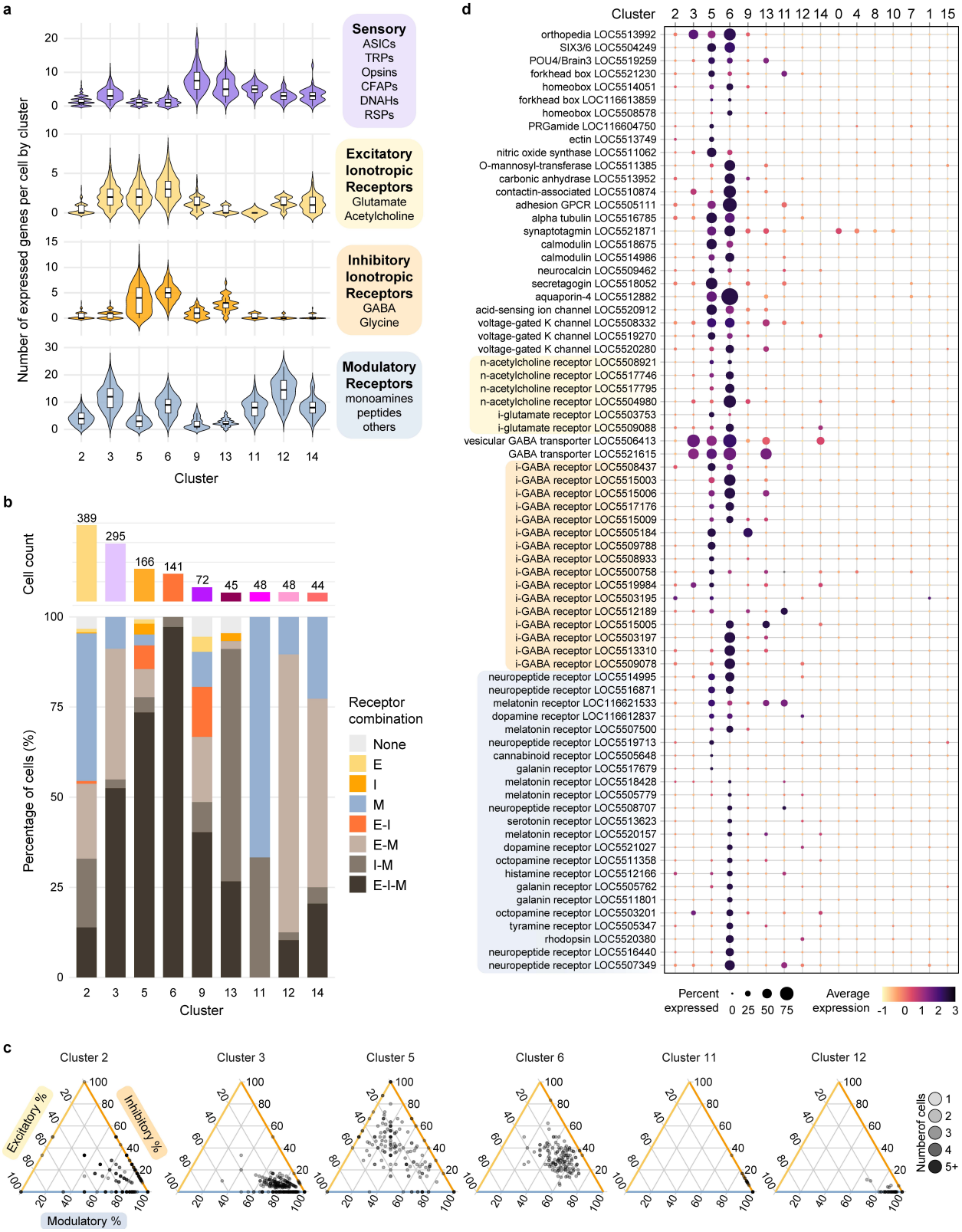

Figure 3 | Integrative receptor repertoires distinguish interneuron-like neural clusters.

(a) Violin plots showing the number of sensory-related and neurotransmitter receptor genes detected per cell across neural clusters. Gene categories are color-coded as sensory (purple), ionotropic excitatory (E, gold), ionotropic inhibitory (I, orange), and metabotropic/modulatory (M, blue). **(b)** Co-expression analysis of E/I/M receptor combinations across neural clusters. The upper histogram shows total cell counts per cluster, and the lower stacked bar plot shows the percentage of cells in each cluster belonging to different receptor-class combination categories. Pale gray denotes cells lacking detectable neurotransmitter receptors; gold, excitatory-only; orange, inhibitory-only; blue, modulatory-only; orange-red, excitatory–inhibitory; light gray, excitatory–modulatory; medium gray, inhibitory–modulatory; and dark gray, cells co-expressing all three receptor classes. **(c)** Ternary plots showing the relative proportions of detected E, I, and M receptors per cell for selected clusters. Each point represents a cell, positioned according to its E/I/M receptor composition. Point color indicates the number of overlapping cells sharing the same receptor ratio, from light gray (1 cell) to black (≥5 cells). **(d)** Dot plot showing expression patterns of transcription factors, synaptic components, ion channels, and neurotransmitter receptors associated with fast neurotransmission and neuromodulation across clusters. Dot size indicates the percentage of cells expressing each gene, and color represents scaled average expression (pale yellow to dark purple). Gold, orange, and blue shading highlight genes belonging to the E, I, and M receptor families, respectively.

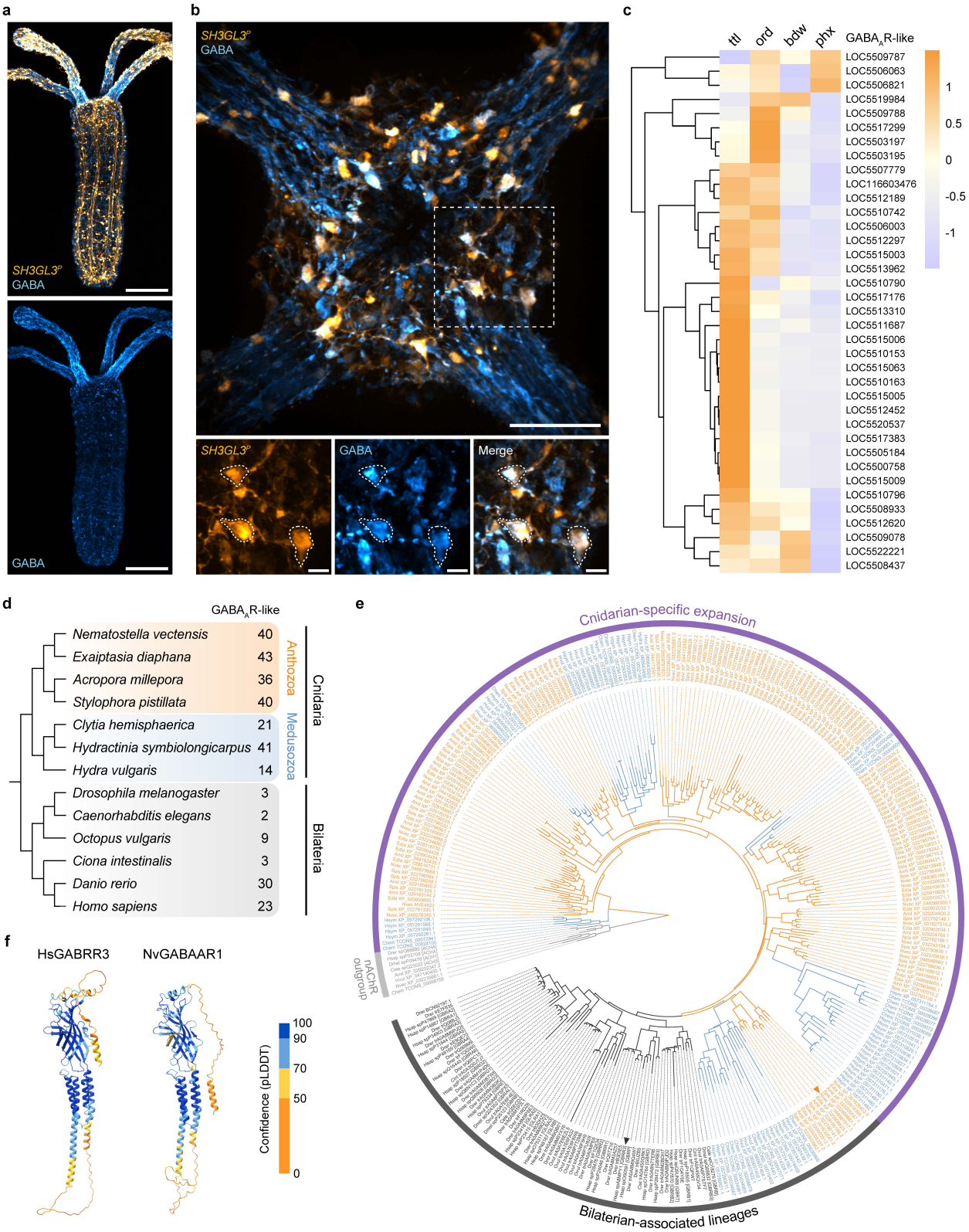

Figure 4 | Expansion and oral enrichment of ionotropic GABAergic signaling components.

1255 **(a)** Whole-mount γ-aminobutyric acid (GABA) immunostaining of
1256 *NvSH3GL3^{P}>mScarlet-I* primary polyps, showing enriched GABA immunoreactivity in
1257 the oral disc and tentacles. Scale bars, 100 µm. **(b)** Within the oral disc, GABA
1258 immunoreactivity is restricted to large-soma cells, including both mScarlet-I-positive
1259 neurons and additional large-soma GABA-positive cells lacking reporter signal. Top,
1260 merged image of *SH3GL3^{P}* (orange) and GABA (blue), with the dashed box indicating
1261 the region shown below. Bottom, split-channel views of the boxed region (*SH3GL3^{P}*,
1262 left; GABA, middle; merge, right). Dashed outlines mark representative large-soma cells
1263 that are double-positive for *SH3GL3^{P}* and GABA. GABA accumulation is also visible in
1264 varicosities along neurites. Scale bars, 50 µm (top), 10 µm (bottom). **(c)** Heatmap
1265 showing tissue-specific expression of GABA type A receptor-like ($GABA_AR$-like)
1266 homologs in adult *Nematostella*. Colors indicate Z-scored average TPM per gene
1267 across tissues (ttl, tentacles; ord, oral disc; bdw, oral body wall; phx, pharynx), with
1268 warmer colors representing higher relative expression. **(d)** Gene counts of $GABA_AR$-like
1269 homologs across seven cnidarian species (four anthozoans, three medusozoans) and
1270 six bilaterian species. Anthozoans (orange) and medusozoans (blue) show marked
1271 expansion of the receptor family relative to bilaterians (dark gray). **(e)** Maximum-
1272 likelihood phylogeny of $GABA_AR$-like homologs based on amino-acid sequences from
1273 the species set in (d). Anthozoan sequences are shown in orange, medusozoan
1274 sequences in blue, and bilaterian sequences in dark gray; representative nicotinic
1275 acetylcholine receptor (nAChR) subunits (light gray) form an outgroup to root the tree.
1276 Outer arcs denote the cnidarian-specific expansion (orange) and the bilaterian-
1277 associated lineage (dark gray). Arrowheads indicate the *Nematostella* subunit
1278 NvGABAAR1 (orange) and the human subunit GABRR3 (dark gray) selected for
1279 structural comparison in (f). Branch support for the cnidarian–bilaterian split was
1280 assessed with ultrafast bootstrap and SH-like aLRT values of 92.3 and 80; full support
1281 values are shown in Supplementary Fig. 1. **(f)** AlphaFold-predicted structures of *Homo*
1282 *sapiens* GABRR3 (γ-aminobutyric acid type A receptor subunit ρ3) and its *Nematostella*
1283 *vectensis* homolog NvGABAAR1 (protein ID: XP_048587017.1; gene ID: LOC5505184),
1284 corresponding to the subunits marked by arrowheads in (e). Ribbon coloring indicates

1285 per-residue model confidence (pLDDT): orange (0–50), yellow (50–70), light blue (70–
1286 90), and dark blue (90–100).
1287

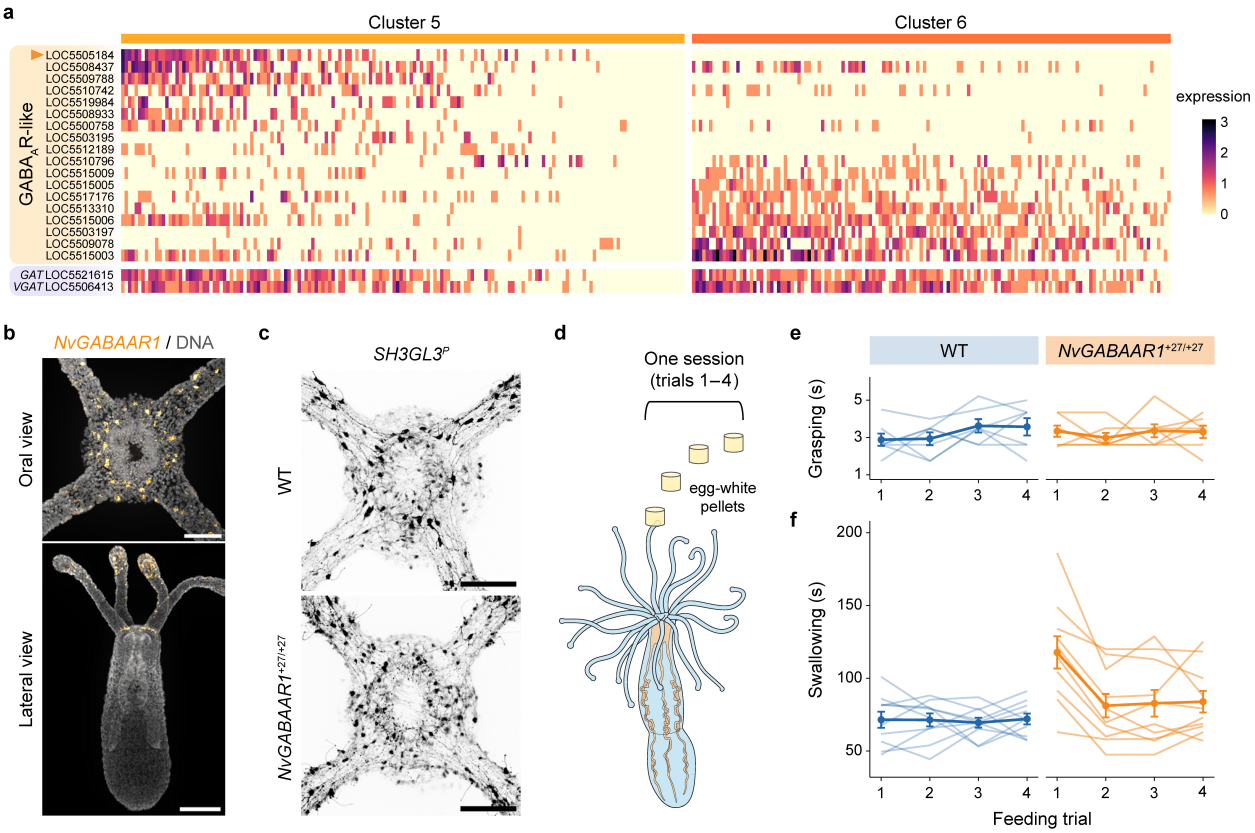

Figure 5 | Loss of *NvGABAAR1* selectively delays swallowing initiation during feeding.

(a) Heatmap showing SCT-normalized expression of genes involved in GABA signaling across single cells from clusters 5 and 6. The gene set includes multiple GABA$_A$R-like subunits as well as the plasma membrane GABA transporter (*GAT*) and vesicular GABA transporter (*VGAT*). Columns represent individual cells ordered within each cluster by aggregate expression of this gene set. Rows are grouped by gene category and arranged from cluster-5-enriched (top) to cluster-6-enriched (bottom). The orange arrowhead marks LOC5505184 (*NvGABAAR1*), the subunit highlighted in Fig. 4e and analyzed functionally in Fig. 5b–f. **(b)** FISH in four-tentacle primary polyps showing *NvGABAAR1* expression restricted to the oral region, including the oral disc and a subset of tentacle neurons. *NvGABAAR1* signal in orange; DNA counterstain in gray. Top, oral view; bottom, lateral view. Scale bars, 50 µm (top), 100 µm (bottom). **(c)** Confocal images of wild-type (WT) and *NvGABAAR1*$^{+27/+27}$ primary polyps in the *NvSH3GL3*^{P}*>mScarlet-I* reporter background. The organization of the oral nerve ring appears comparable at the level of gross morphology between WT and mutants. Scale

1305 bars, 50 μm. **(d)** Feeding assay design. Each behavioral session consisted of four
1306 sequential presentations of 1 mm × 1 mm egg-white pellets delivered to the oral disc.
1307 **(e)** Grasping duration across four feeding trials using pipette-delivered food pellets. Thin
1308 lines represent individual animals (WT in blue, n = 7; *NvGABAAR1*$^{+27/+27}$ mutants in
1309 orange, n = 7); bold lines and error bars denote mean ± s.e.m. Grasping duration was
1310 comparable between genotypes. **(f)** Swallowing duration across four feeding trials.
1311 Animals were assayed using either pipette or whisker delivery (each animal was tested
1312 with a single method throughout its session). Delivery method did not affect the
1313 genotype × trial interaction (see Methods), so data were analyzed together. Thin lines
1314 represent individual animals (WT in blue, n = 10; mutants in orange, n = 10); bold lines
1315 and error bars denote mean ± s.e.m. Mutants exhibited a pronounced increase in
1316 swallowing duration on trial 1 (46.6 ± 10.1 s; p = 0.0001) but converged to WT-like
1317 performance on trials 2–4. Full statistical details are provided in Supplementary Table 5.
1318

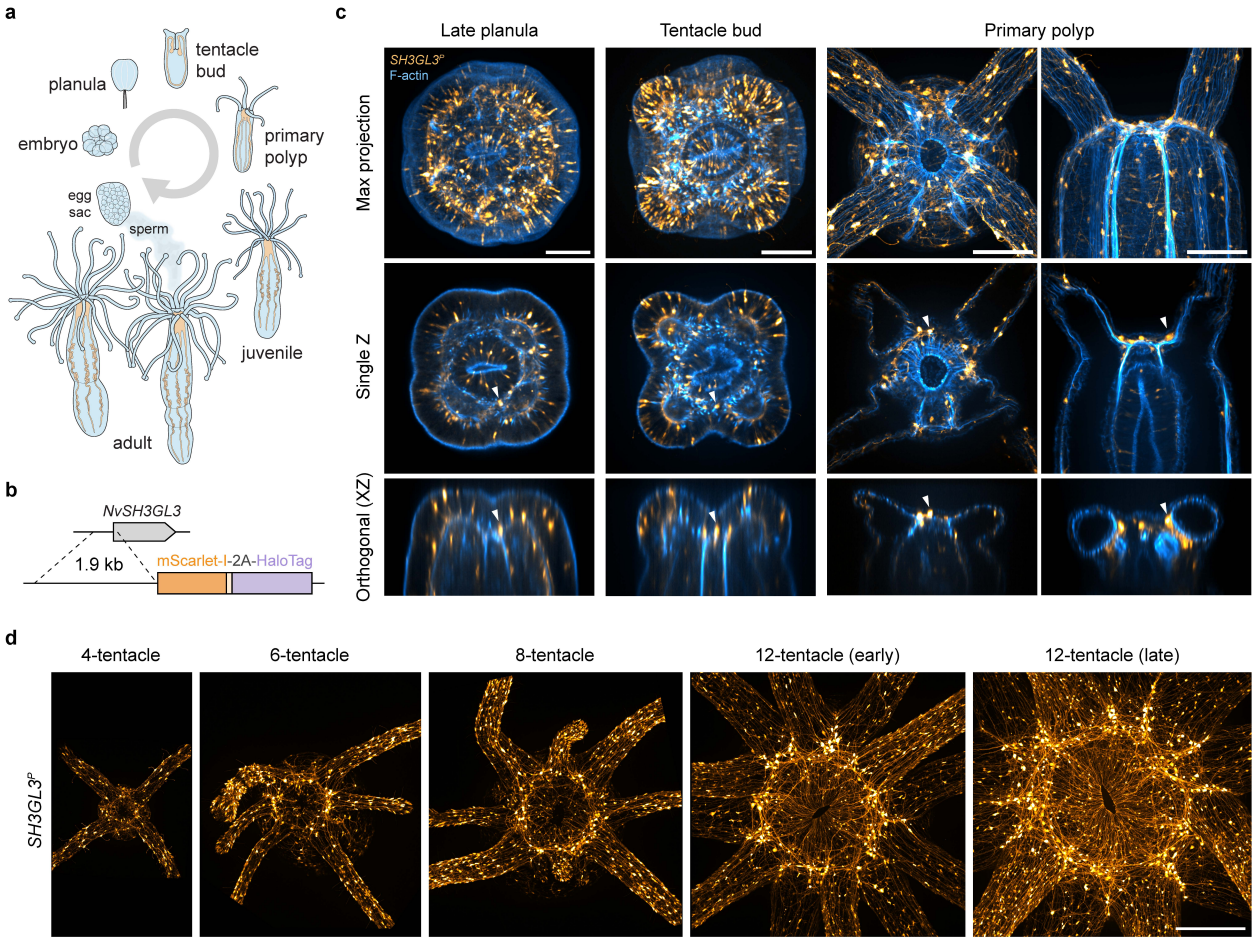

Extended Data Figure 1 | Developmental emergence and scaling of the oral nerve ring

(a) Schematic overview of *Nematostella vectensis* life stages, from embryo to adult, indicating the progressive addition of tentacles and the transition from planula larva to primary polyp and juvenile stages. **(b)** Schematic of the *NvSH3GL3*^{P} reporter construct. A 1.9 kb upstream regulatory region of *NvSH3GL3* drives expression of an mScarlet-I fluorescent reporter used to visualize neuronal morphology. **(c)** Confocal images showing *NvSH3GL3*^{P}*>mScarlet-I*–labeled neurons (orange) across early developmental stages, with F-actin staining (blue). Columns show late planula larvae (3.5 dpf), tentacle buds (4.5 dpf), and primary polyps (10 dpf). Rows show maximum intensity projections (top), single optical sections (middle), and orthogonal (XZ) views (bottom). Late planula and tentacle-bud stages are shown in oral view, whereas primary polyps are shown in both oral and lateral views. In late planulae, sparsely distributed neurons with enlarged somata are observed in basal positions within the oral ectoderm. As tentacles emerge

1334 during the tentacle-bud and primary polyp stages, the number of these large-soma
1335 neurons increases, accompanied by higher neurite density and localization to the
1336 ectoderm at tentacle junctions. White arrowheads indicate representative neuronal
1337 somata shown in corresponding single optical sections and orthogonal views. Scale
1338 bars, 50 μm. **(d)** Oral-view maximum intensity projections showing
1339 *NvSH3GL3*^{P}*>mScarlet-I*–labeled neurons (orange) in polyps with increasing tentacle
1340 number (4, 6, 8, and 12). As polyps grow and sequentially add tentacles, the
1341 circumorally projecting neurite bundle that constitutes the oral nerve ring (ONR)
1342 becomes progressively denser, accompanied by increased accumulation of large
1343 neuronal somata at tentacle junctions. All panels are shown at the same scale. Scale
1344 bar, 200 μm.
1345

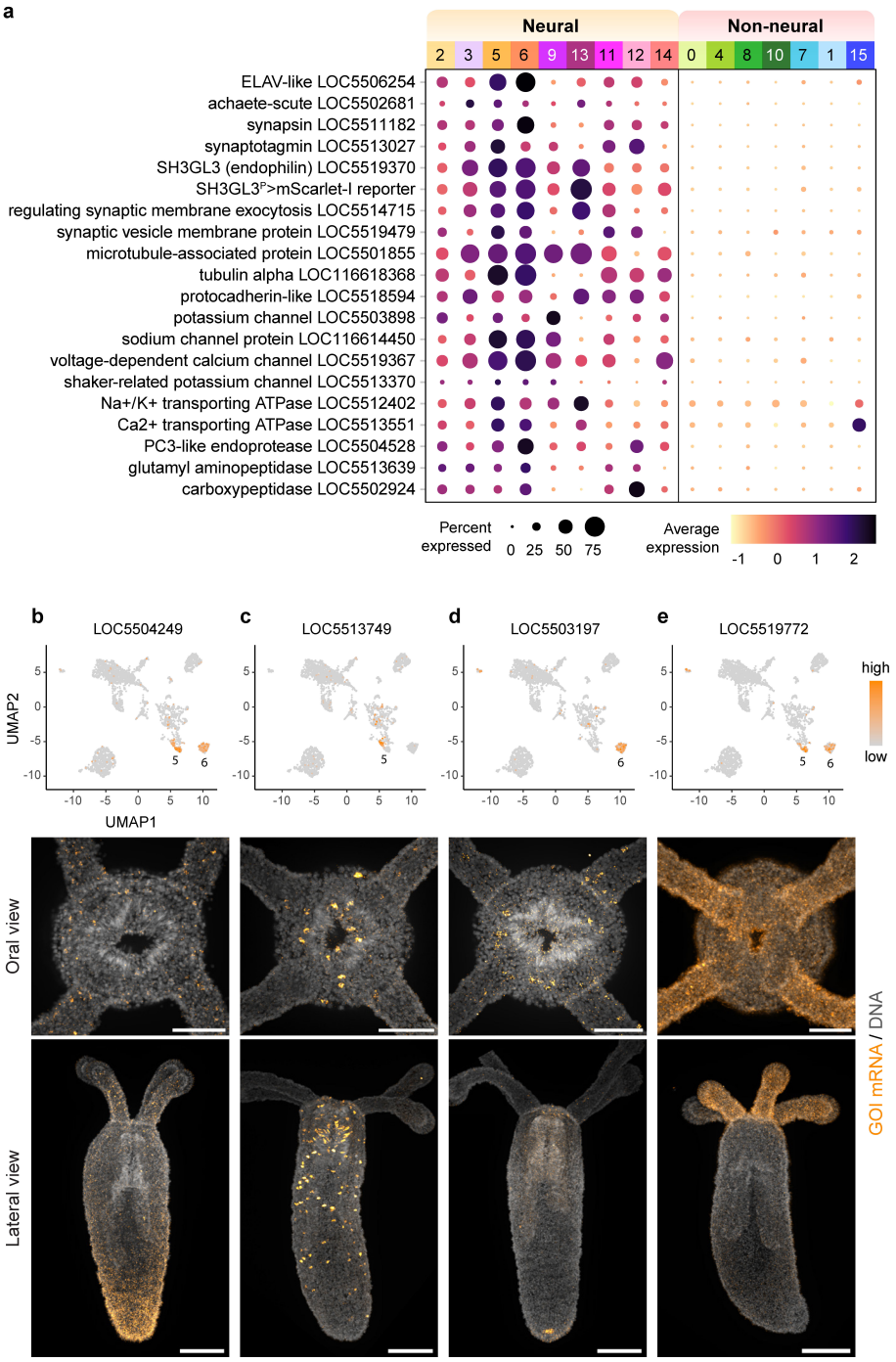

Extended Data Figure 2 | Molecular and spatial validation of oral neuronal cluster identities

(a) Dot plot showing expression of canonical neuronal markers, synaptic machinery, ion channels, cytoskeletal components, and signaling enzymes across neural and non-neural clusters. Dot size indicates the percentage of cells expressing each gene, and color denotes scaled average expression. **(b–e)** Representative fluorescent in situ

1353 hybridization (FISH) analyses in four-tentacle primary polyps (7–10 days post-
1354 fertilization) for genes enriched in clusters 5 and 6 that did not meet criteria for ONR
1355 markers. Shown are examples of transcripts that are weak or undetectable at this stage
1356 (b), expressed in the body column (c,d), or diffusely distributed across oral tissues
1357 without enrichment in ONR-like neurons (e). Oral (top) and lateral (bottom) views are
1358 shown for each FISH experiment. DNA is shown in gray and gene-specific signal in
1359 orange. Scale bars, 50 μm (oral views) and 100 μm (lateral views).
1360

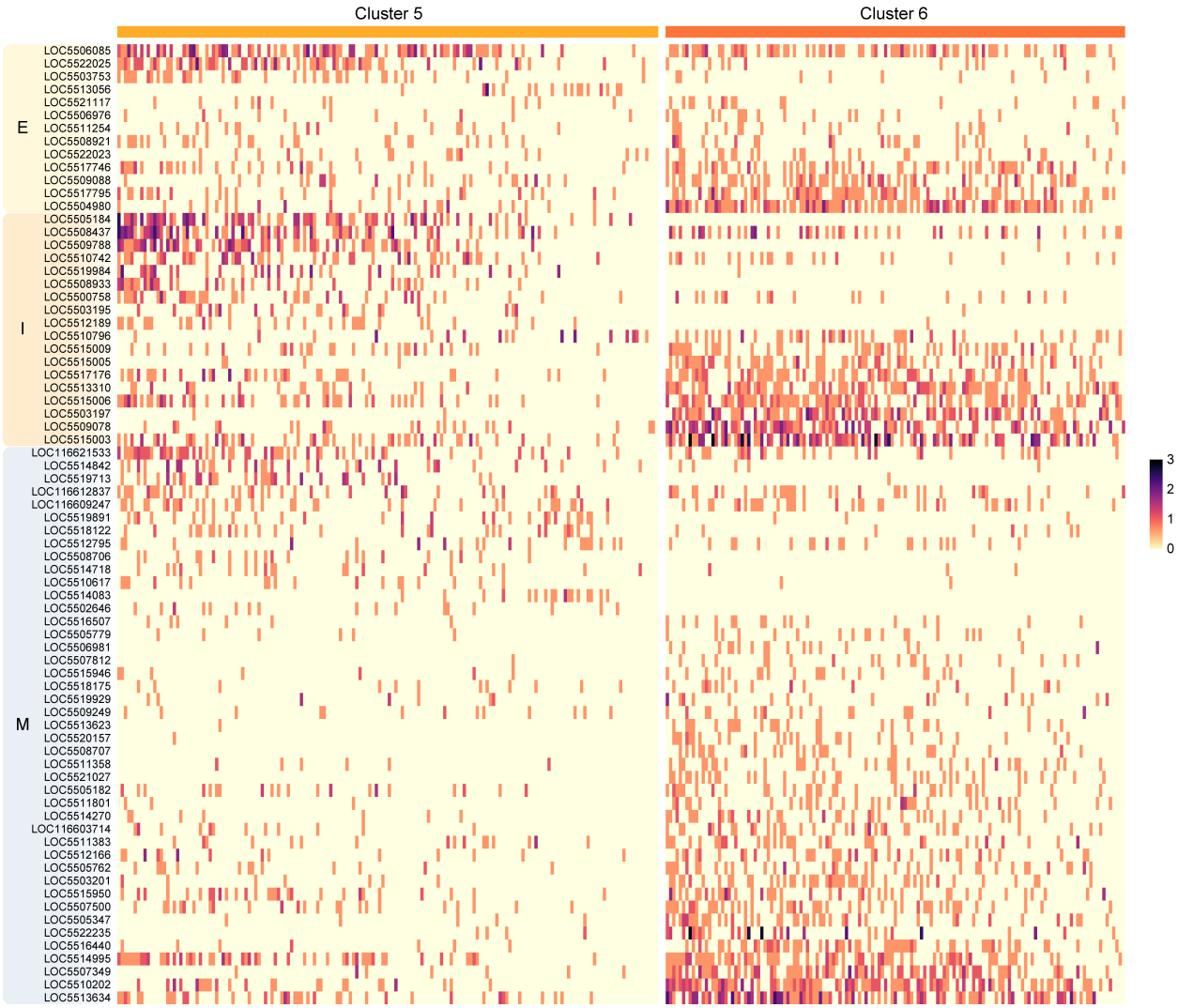

Extended Data Figure 3 | Neurotransmitter receptor family expression across interneuron-like clusters.

Heatmap showing SCT-normalized expression of excitatory (E), inhibitory (I), and modulatory (M) neurotransmitter receptor genes across individual cells from clusters 5 and 6. Columns represent single cells, ordered within each cluster by aggregate expression of the displayed receptor set. Rows represent receptor genes, grouped by gene category and arranged from cluster-5-enriched (top) to cluster-6-enriched (bottom). Color indicates SCT-normalized expression (see color bar). This analysis provides gene-level context for the integrative receptor repertoires summarized in Fig. 3a–c and for the inhibitory signaling components examined in Fig. 5a.

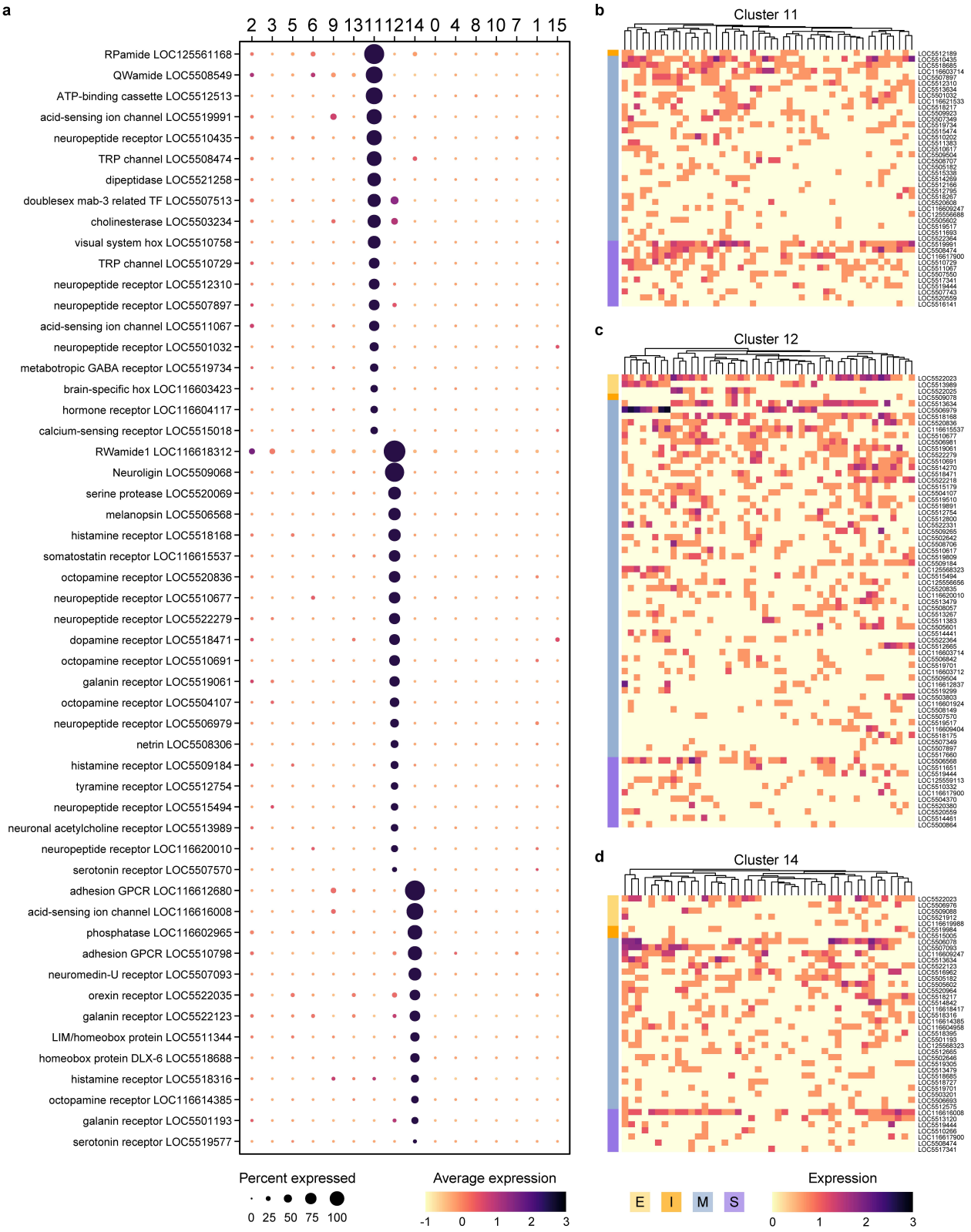

Extended Data Figure 4 | Molecular features of modulatory and sensory-enriched neuronal clusters.

(a) Dot plot showing expression of marker genes enriched in clusters 11, 12, and 14. Dot size indicates the percentage of cells expressing each gene, and color represents scaled average expression (pale yellow to dark purple). **(b–d)** Heatmaps showing SCT-normalized expression of cluster-enriched genes in clusters 11 (b), 12 (c), and 14 (d). Columns represent individual cells ordered by hierarchical clustering within each cluster, and rows represent genes grouped by functional category. Gene groups are color-coded as ionotropic excitatory (gold), ionotropic inhibitory (orange), metabotropic/modulatory (blue), and sensory (purple).

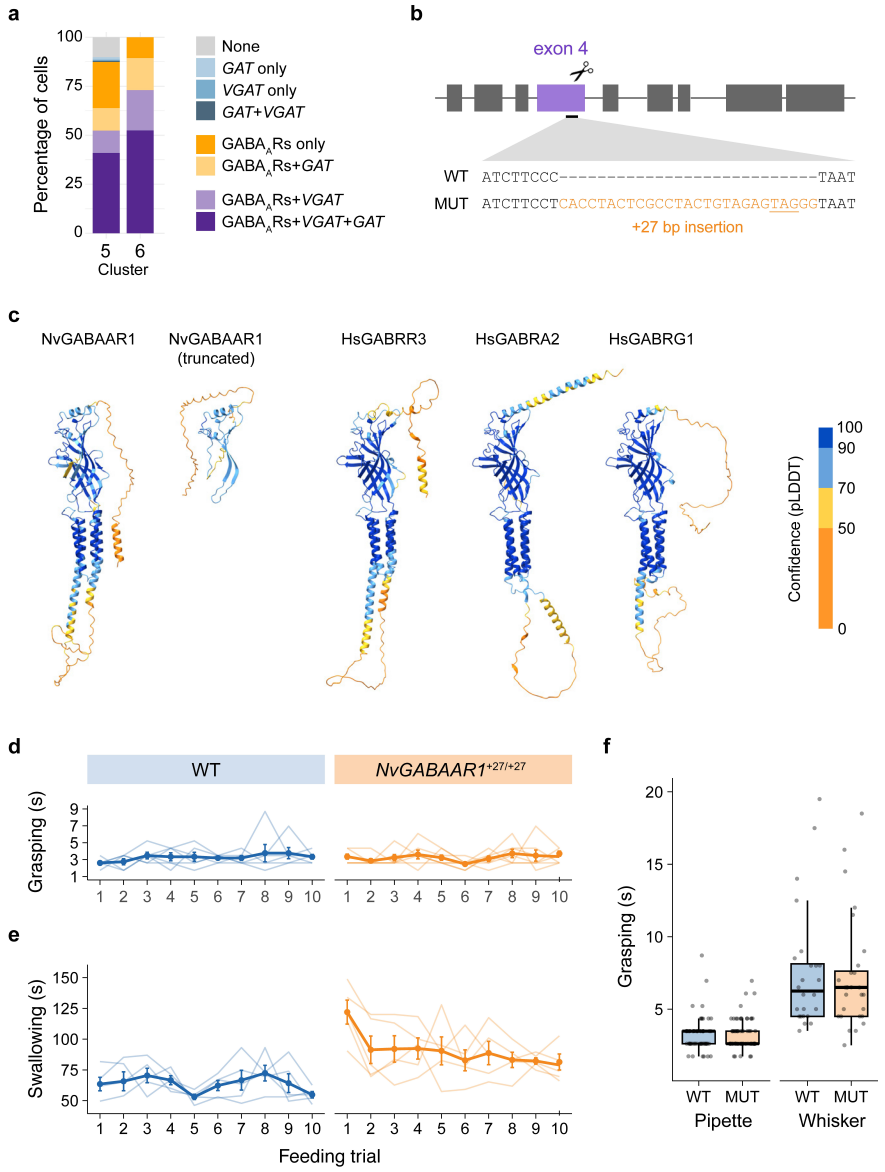

Extended Data Figure 5 | Molecular context, mutant design, and extended analysis of *NvGABAAR1*$^{+27/+27}$ feeding behavior.

(a) Stacked bar plot showing the percentage of cells in clusters 5 and 6 expressing combinations of γ-aminobutyric acid (GABA) pathway components, including GABA type A receptor-like (GABA$_A$R-like) subunits, the vesicular GABA transporter (*VGAT*), and the plasma membrane GABA transporter (*GAT*). This analysis complements the single-cell-level expression patterns shown in Fig. 5a. “None” indicates cells lacking detectable expression of all three components. For brevity, GABA$_A$Rs in the color key refer to GABA$_A$R-like subunits. Colors denote distinct co-expression categories: gray, none; light blue, *GAT* only; blue, *VGAT* only; dark blue, *GAT* + *VGAT*; orange,

1396 $GABA_A$Rs only; light orange, $GABA_A$Rs + *GAT*; lavender, $GABA_A$Rs + *VGAT*; and
1397 purple, $GABA_A$Rs + *VGAT* + *GAT*. **(b)** Schematic of the *NvGABAAR1*$^{+27}$ allele.
1398 CRISPR/Cas9 targeting in exon 4 introduced a 27-bp insertion (orange), resulting in a
1399 frameshift and a premature stop codon (underlined). **(c)** AlphaFold-predicted structures
1400 of the full-length *Nematostella vectensis* $GABA_A$ receptor-like subunit NvGABAAR1, the
1401 truncated NvGABAAR1 protein generated by the +27-bp frameshift mutation shown in
1402 (b), together with representative human $GABA_A$ receptor subunits (HsGABRR3,
1403 HsGABRA2, and HsGABRG1), shown in addition to the structures presented in Fig. 4f.
1404 Structures are displayed as ribbon models and colored by per-residue model confidence
1405 (pLDDT), from low (orange) to high (blue). This comparison highlights the structural
1406 consequence of NvGABAAR1 truncation and illustrates the range of structural diversity
1407 among human $GABA_A$ receptor subunits. **(d)** Grasping duration across ten sequential
1408 feeding trials per animal in wild-type (WT; blue, n = 6) and *NvGABAAR1*$^{+27/+27}$ mutants
1409 (orange, n = 7), using pipette-delivered food pellets. Each thin line represents an
1410 individual animal; thick lines show the mean ± s.e.m. **(e)** Swallowing duration across ten
1411 sequential feeding trials per animal in wild-type (n = 5) and *NvGABAAR1*$^{+27/+27}$ mutants
1412 (n = 5), using pipette-delivered food pellets. Each thin line represents an individual
1413 animal; thick lines show the mean ± s.e.m. **(f)** Grasping duration for WT (blue) and
1414 *NvGABAAR1*$^{+27/+27}$ mutants (orange) under two pellet-delivery conditions. Pipette: WT
1415 (n = 6 animals, 60 trials) and mutants (n = 7 animals, 70 trials). Whisker: WT (n = 4
1416 animals, 24 trials) and mutants (n = 5 animals, 28 trials). Each point represents an
1417 individual trial. Boxplots show the median (horizontal line) and interquartile range (IQR;
1418 25th–75th percentile), with whiskers extending to the most extreme data points within
1419 1.5× the IQR. All data points are plotted as horizontally jittered points.
1420